Frequency-Dependent *F*-Number Suppresses Grating Lobes and Improves the Lateral Resolution in Coherent Plane-Wave Compounding

Martin F. Schiffner, *Graduate Student Member, IEEE*, and Georg Schmitz, *Senior Member, IEEE*

***Abstract*—Ultrafast imaging modes, such as coherent plane-wave compounding (CPWC), increase image uniformity and reduce grating lobe artifacts by dynamic receive apertures. The focal length and the desired aperture width maintain a given ratio, which is called the *F*-number. Fixed *F*-numbers, however, exclude useful low-frequency components from the focusing and reduce the lateral resolution. Herein, this reduction is avoided by a frequency-dependent *F*-number. This *F*-number derives from the far-field directivity pattern of a focused aperture and can be expressed in closed form. The *F*-number, at low frequencies, widens the aperture to improve the lateral resolution. The *F*-number, at high frequencies, narrows the aperture to avoid lobe overlaps and suppress grating lobes. Phantom and in vivo experiments with a Fourier-domain beamforming algorithm validated the proposed *F*-number in CPWC. The lateral resolution, which was measured by the median lateral full-widths at half-maximum of wires, improved by up to 46.8% and 14.9% in a wire and a tissue phantom, respectively, in comparison to fixed *F*-numbers. Grating lobe artifacts, which were measured by the median peak signal-to-noise ratios of wires, reduced by up to 9.9 dB in comparison to the full aperture. The proposed *F*-number thus outperformed *F*-numbers that were recently derived from the directivity of the array elements.**

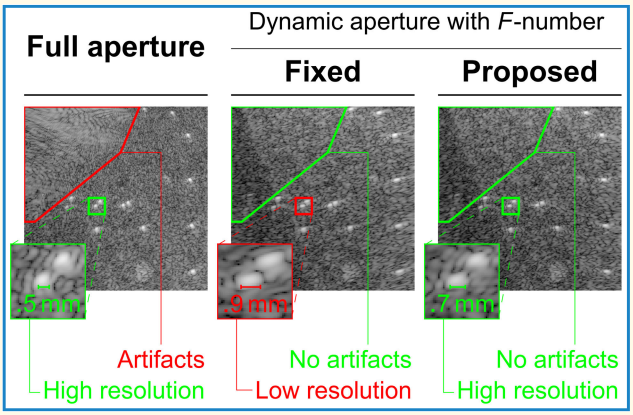

***Index Terms*— Dynamic aperture, *F*-number, Fourier-domain beamforming, frequency-dependent apodization, grating lobes, ultrafast ultrasound imaging.**

I. Introduction

ULTRAFAST ultrasound imaging (UI) modes, such as coherent plane-wave compounding (CPWC) [1], [2], [3] or synthetic aperture (SA) imaging [4], capture large fields of view (FOVs) at kilohertz rates [5]. These rates result from a combination of unfocused waves, which insonify the entire FOV at each emission, and fully sampled transducer arrays. A single pulse-echo measurement provides enough data to form a low-quality image. The image formation is based upon software [2], [5] and usually applies the delay-and-sum (DAS) algorithm [6]. This algorithm uses receive focusing to determine the echogenicity of all volume elements (voxels) in the image. This algorithm, moreover, enables the superposition of the low-quality images to synthesize transmit foci in retrospect and improve the image quality at the expense of the frame rate.

Linear arrays, as shown in Fig. 1, are among the most popular probe types [7], [8]. These arrays facilitate the imaging of superficial structures, such as the peripheral vasculature [9] or parts of the musculoskeletal system [10], and small organs [11]. The arrays widen the FOV near the skin surface by a large element pitch p_e of the order of the center wavelength λ_c (i.e., $p_e \approx \lambda_c$) [6], [12]. This element pitch reduces the number of elements in a given footprint and, thus, system complexity and costs [13]. The element pitch, however, also violates the sampling theorem and produces grating lobes. Such lobes reduce the dynamic range available for unambiguous imaging and can result in multiple images of the same reflector [14, p. 438], [15]. Echoes from the grating lobe

Manuscript received 18 May 2023; accepted 26 June 2023. Date of publication 3 July 2023; date of current version 29 August 2023. *(Corresponding author: Martin F. Schiffner.)*

This work involved human subjects or animals in its research. Approval of all ethical and experimental procedures and protocols was granted by the Ethics Board of Ruhr University Bochum under Registration No. 4433-12.

The authors are with the Chair of Medical Engineering, Ruhr University Bochum, 44780 Bochum, Germany (e-mail: martin.schiffner@rub.de; georg.schmitz@rub.de).

Digital Object Identifier 10.1109/TUFFC.2023.3291612

Highlights

- **A frequency-dependent *F*-number is enabled by translating delay-and-sum beamforming into the Fourier domain and selecting the receive aperture as a function of both the focus and the frequency.**
- **The frequency-dependent *F*-number reduces image artifacts to a similar extent as a fixed *F*-number but, owing to wider apertures at low frequencies, improves significantly the lateral resolution.**
- **Frequency dependence of the *F*-number is easy to implement and can improve the lateral resolution of all delay-and-sum-based imaging modes (e.g., synthetic aperture imaging or line-by-line scanning).**

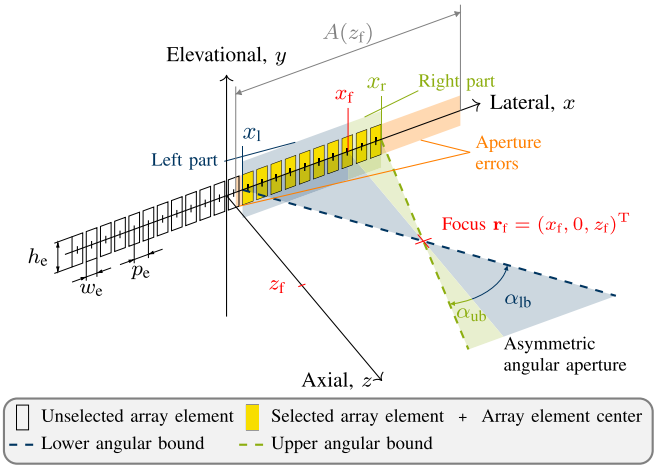

Fig. 1. Selection of the receive aperture. The DAS algorithm first uses the focal length z_f and the *F*-number (1) to compute the desired aperture width $A(z_f) = z_f/F$. The algorithm then selects all array elements whose lateral center coordinates lie within a distance of $A(z_f)/2$ from the lateral focal coordinate x_f. These selected elements form the aperture. This aperture has left and right bounds x_l and x_r that coincide with the left and right edges of specific array elements and usually differ from the desired bounds $x_f - A(z_f)/2$ and $x_f + A(z_f)/2$ (gray lines), respectively. Such differences are aperture errors (shaded orange). In the illustrated case, the positioning of the focus near the right edge of the array causes an asymmetric aperture in which the right part (shaded green) is narrower than the left part (shaded blue). The left part, however, is also too narrow because the desired left bound $x_f - A(z_f)/2$ lies between the left edge of an array element and an array element center. These errors also affect the angular aperture (i.e., $|\alpha_{lb}| > \alpha_{ub}$).

locations are mistaken for echoes from the focus. Ultrafast UI, due to the insonification of the entire FOV, is more susceptible to this mistake than line-by-line scanning [16], [17].

The DAS algorithm, as shown in Fig. 1, uses a technique known as dynamic receive aperture to increase image uniformity [14, Table 7.3] and reduce grating lobe artifacts [13], [17], [18]. This technique ensures that the receive focusing, for any given focus $\mathbf{r}_f = (x_f, 0, z_f)^T$, processes only those echoes that are received by a specific set of array elements. This set, which will be called "receive aperture," is dynamic because, ideally, it is centered on the lateral focal coordinate x_f and increases linearly in width with the focal length z_f. The focal length z_f and the desired aperture width $A(z_f)$, hence, maintain a given ratio, which is known as the *F*-number [3, eq. (3)], [6, Sec. 2.D], [14, p. 173], [17, eq. (12)]

$$F = \frac{z_f}{A(z_f)} \tag{1}$$

and typically ranges from 0.75 to 2 [1], [2], [3], [6], [8], [19, p. 414]. Dynamic apertures, however, reduce the lateral resolution [8], [14, Table 7.3], [20]. The aperture formation from the discrete array elements, moreover, causes aperture errors (see Fig. 1). These errors include miscentering, deviations from the desired width, and asymmetry.

Little information is available about the physics of dynamic apertures, the optimal value of the *F*-number (1), and the effect of any aperture errors. Delannoy et al. [17] and Bruneel et al. [18] showed analytically that the *F*-number (1) controls the grating lobe level (GLL) (i.e., the ratio of the maximum amplitudes attained by the grating lobes and the main lobe) of the monofrequent receive beam in the focal plane. The analysis, however, used the Fresnel approximation, which is only valid near the focus [21, Sec. 4.7], and obsolete array geometries. Wilcox and Zhang [13] studied numerically the effect of the grating lobes on the point spread function (PSF) in SA imaging. Although the study validated an empirical rule for the selection of the *F*-number, the physical reasons and the scope of validity remain unclear.

Jensen et al. [1], Montaldo et al. [3], Perrot et al. [6], and Szabo [19, Sec. 10.12.2] ignored the effect of the *F*-number (1) on the GLL and justified the usage of a dynamic receive aperture and the typical values of the *F*-number (1) with the suppression of measurement noise. This noise has similar power in all receive channels. An echo from the focus, in contrast, arrives at each array element at a different angle α with respect to the normal and generates a signal power that decreases as a function of this angle because the array elements have a directivity $D(\alpha)$. This directivity, in the far-field, equals the product of an obliquity factor $o(\alpha)$ and a sinc function, i.e., [14, Sec. 7.2.5], [19, Sec. 7.7]

$$D(\alpha) = o(\alpha)\,\mathrm{sinc}\left[\sin(\alpha)\frac{w_e}{\lambda}\right] \tag{2}$$

where $o(\alpha) = \cos(\alpha)$ for a soft baffle, $o(\alpha) = 1$ for a rigid baffle, $\mathrm{sinc}(x) = \sin(\pi x)/(\pi x)$, and w_e/λ is the element width-to-wavelength ratio. To ensure that all processed echoes have sufficient signal-to-noise ratios (SNRs), the authors thresholded the directivity (2) to derive a maximum acceptance angle $\hat{\alpha} \in (0; \pi/2)$ and, using the relation $F = 1/[2\tan(\hat{\alpha})]$ [6, eq. (12)], an *F*-number. Such directivity-derived *F*-numbers, however, are deficient because they ignore other sources of attenuation, such as absorption or diffraction, and, more importantly, grating lobes. These lobes, in standard UI systems, create stronger image artifacts than the noise.

All above studies suggest that the *F*-number (1) should increase monotonically with the frequency f. Such frequency dependence, which will be denoted by $F(f)$, describes a dynamic aperture that not only varies with the focus $\mathbf{r}_f$ but also narrows with the frequency f. The DAS algorithm,

however, requires a fixed F-number and typically uses the values at the center frequency f_c (i.e., $F = F(f_c)$, see [13], [19, Sec. 10.12.2]) or the upper frequency bound f_{ub} (i.e., $F = F(f_{ub})$, see [6]). Such fixed F-numbers are suboptimal. The maximum value at the upper frequency bound $F(f_{ub})$, for example, uses the narrowest aperture for all lower frequencies and, thus, reduces unnecessarily the lateral resolution. Clinical images, however, must discern the smallest possible dimensions [8].

This article reminds the reader that dynamic receive apertures suppress grating lobes and proposes two innovations. First, frequency dependence of the F-number (1) is incorporated into the image formation. This incorporation is achieved by translating the receive focusing, which the DAS algorithm usually performs in the time domain, into the Fourier domain and making the aperture selection dependent on both the focus and the frequency. Second, a closed-form expression for a frequency-dependent F-number is proposed that maximizes the lateral resolution under two constraints on the grating lobes. Both constraints derive from the far-field directivity pattern of a focused aperture and limit the GLL to make a minimum dynamic range available for unambiguous imaging. Phantom and in vivo experiments show that the proposed F-number not only improves the lateral resolution in comparison to fixed F-numbers (1) but also outperforms two directivity-derived F-numbers in the reduction of image artifacts. This article significantly extends our previous work [22]. The extensions include: 1) a description of the Fourier-domain receive focusing; 2) the treatment of aperture errors; 3) a derivation of the far-field directivity pattern using the method of stationary phase; and 4) additional experiments.

II. Theory

The Fourier-domain receive focusing, which incorporates a frequency-dependent F-number $F(f)$, will be presented first. This kind of focusing will subsequently be used to derive the far-field directivity pattern of a focused aperture and the proposed F-number. All derivations make the following assumptions. The linear array, according to the Cartesian coordinate system in Fig. 1, has N_e elements of width w_e and height h_e. Their center coordinates are

$$x_{e,m} = (m - M_e)\,p_e \quad \text{and} \quad y_{e,m} = z_{e,m} = 0 \tag{3}$$

for all element indices $m \in \mathbb{M} = \{0, 1, \ldots, N_e - 1\}$, where $M_e = (N_e - 1)/2$ and $p_e > w_e$ is the element pitch. The mth element, in each pulse-echo measurement, acquires the radio frequency (RF) signal $u_m(t)$, where t is the time elapsed since the transmission of a plane wave (PW) at $t = 0$. Each signal $u_m(t)$ is assumed to be analytic [19, Sec. A.2.7] and bandpass band-limited (i.e., there are lower and upper bounds $f_{lb} > 0$ and $f_{ub} > f_{lb}$, respectively, such that the signal has energy only in the range of frequencies $f_{lb} \le f \le f_{ub}$). The acquired RF signals $u_m(t)$ are processed in software to form an image whose voxels are located on a regular grid in the xz plane (i.e., $y = 0$).

A. Proposed Fourier-Domain Receive Focusing

The receive focusing estimates the pulse echoed by a single image voxel, which is located at the focus $\mathbf{r}_f$, by summing coherently the acquired RF signals $u_m(t)$ [3, eq. (2)], [6, eq. (9)], [13, eq. (1)]. These signals, however, result from superposition of tens of thousands of spherical waves at the array elements. Each wave emanates from an image voxel upon insonification by the transmitted PW. Each signal $u_m(t)$, thus, contains not only the desired pulse but, aside from measurement noise, also interference (i.e., undesired pulses echoed by the image voxels away from the focus $\mathbf{r}_f$). The coherent summation produces a focused RF signal $u^{(foc)}(\mathbf{r}_f, t)$ in which the desired pulse is usually amplified compared to the noise and the interference. The interference from specific voxels, however, adds up constructively and, if their echogenicity is high, obscures the desired pulse. This applies to voxels near the focus $\mathbf{r}_f$ and at the grating lobe locations due to limited spatial resolution and too large an element pitch, respectively. The influence of both causes will be balanced for each frequency by expressing the focused RF signal $u^{(foc)}(\mathbf{r}_f, t)$ in the Fourier domain [23] and using a frequency-dependent F-number $F(f)$. The resulting dynamic aperture, which varies not only with the focus $\mathbf{r}_f$ but also with the frequency f (see Section I), will be described by a set $\mathbb{A}(\mathbf{r}_f, f) \subseteq \mathbb{M}$ of element indices.

The focused RF signal $u^{(foc)}(\mathbf{r}_f, t)$ has a finite time duration T_{foc} and, due to the band limits of the acquired RF signals $u_m(t)$, can be represented by the Fourier sum [24, eq. (2.12)]

$$u^{(foc)}(\mathbf{r}_f, t) \approx \sum_{\nu=\nu_{lb}}^{\nu_{ub}} U^{(foc)}(\mathbf{r}_f, f_\nu) e^{j2\pi f_\nu t} \tag{4}$$

where j is the imaginary unit, $f_\nu = \nu / T_{foc}$ are the discrete frequencies, $\nu_{lb} > 0$ and $\nu_{ub} > \nu_{lb}$ are the lower and upper frequency indices, respectively, and $U^{(foc)}(\mathbf{r}_f, f_\nu)$ are the Fourier coefficients. These coefficients derive from the coherent summation in the time domain. This summation, as explained in [3, eq. (2)], [6, eq. (9)], and [13, eq. (1)], is a two-stage process. First, the acquired RF signals $u_m(t)$ are shifted in time to correct any differences in the arrival times $\Delta t_m(\mathbf{r}_f)$ of the spherical wave from the focus $\mathbf{r}_f$ at the individual array elements and align the desired pulses. These time shifts, by the translation rule [25, eq. (2.18)], correspond to shifting in phase the Fourier coefficients of the acquired RF signals [24, eq. (2.13)]

$$U_m(f) = \frac{1}{T_{foc}} \int_0^{T_{foc}} u_m(t) e^{-j2\pi f t} \mathrm{d}t \tag{5}$$

by using the factors $e^{j2\pi f \Delta t_m(\mathbf{r}_f)}$, where the frequency f replaced the discrete frequencies f_ν to simplify the notation. Second, the shifted RF signals $u_m[t + \Delta t_m(\mathbf{r}_f)]$ are weighted in amplitude, a process known as "apodization" [14, Sec. 7.2.9], and summed. This weighted summation, due to the linearity of the Fourier analysis, corresponds to

$$U^{(foc)}(\mathbf{r}_f, f) = \sum_{m=0}^{N_e-1} w_m(\mathbf{r}_f, f) U_m(f) \tag{6}$$

where the complex-valued apodization weights

$$w_m(\mathbf{r}_f, f) = \bar{a}_m(\mathbf{r}_f, f) e^{j2\pi f \Delta t_m(\mathbf{r}_f)} \tag{7}$$

combine the phase shifts with frequency-dependent versions $\bar{a}_m(\mathbf{r}_f, f)$ of the time-domain apodization weights. These

weights implement the dynamic aperture by masking all array elements outside the set $\mathbb{A}(\mathbf{r}_\mathrm{f}, f)$ [i.e., $\bar{a}_m(\mathbf{r}_\mathrm{f}, f) = 0$ for all $m \notin \mathbb{A}(\mathbf{r}_\mathrm{f}, f)$]. The selection of the set $\mathbb{A}(\mathbf{r}_\mathrm{f}, f)$ and the computations of both the weights $\bar{a}_m(\mathbf{r}_\mathrm{f}, f)$ and the arrival times $\Delta t_m(\mathbf{r}_\mathrm{f})$ within the aperture will now be detailed. Of special interest will be the treatment of aperture errors and a lower bound $z_{\mathrm{f,lb}}$ on the focal length z_f (i.e., $z_\mathrm{f} > z_{\mathrm{f,lb}}$).

1) Dynamic Aperture: The receive aperture has the desired width $A(z_\mathrm{f}, f) = z_\mathrm{f}/F(f)$ and, adapting the selection method in Fig. 1, consists of all array elements whose lateral center coordinates $x_{\mathrm{e},m}$ lie within a distance of $A(z_\mathrm{f}, f)/2$ from the lateral focal coordinate x_f. These elements have the indices[1]

$$\mathbb{A}(\mathbf{r}_\mathrm{f}, f) = \left\{ m \in \mathbb{M} : \left| x_{\mathrm{e},m} - x_\mathrm{f} \right| \leq \frac{z_\mathrm{f}}{2\ F(f)} \right\} \tag{8}$$

for any given values of the focus $\mathbf{r}_\mathrm{f} = (x_\mathrm{f}, 0, z_\mathrm{f})^\mathrm{T}$ and the frequency f. The left and right aperture bounds $x_\mathrm{l}(\mathbf{r}_\mathrm{f}, f)$ and $x_\mathrm{r}(\mathbf{r}_\mathrm{f}, f)$ coincide with the left and right edges of the leftmost and rightmost array elements in (8), respectively, and read

$$x_\mathrm{l}(\mathbf{r}_\mathrm{f}, f) = \left[\min\{\mathbb{A}(\mathbf{r}_\mathrm{f}, f)\} - M_\mathrm{e} \right] p_\mathrm{e} - \frac{w_\mathrm{e}}{2} \tag{9a}$$

$$x_\mathrm{r}(\mathbf{r}_\mathrm{f}, f) = \left[\max\{\mathbb{A}(\mathbf{r}_\mathrm{f}, f)\} - M_\mathrm{e} \right] p_\mathrm{e} + \frac{w_\mathrm{e}}{2} \tag{9b}$$

where the dependence on the focus $\mathbf{r}_\mathrm{f}$ and the frequency f will from now on be omitted to simplify the notation. Any deviations of the lateral bounds (9) from the desired bounds (i.e., $x_\mathrm{l} \neq x_\mathrm{f} - A(z_\mathrm{f}, f)/2$ or $x_\mathrm{r} \neq x_\mathrm{f} + A(z_\mathrm{f}, f)/2$) are aperture errors. These errors, which are usually ignored by the DAS algorithm [3], [6], [13], can be described by two additional F-numbers. These F-numbers will be called "actual F-numbers" and will be shown in Section II-B to determine key properties of the far-field directivity pattern of the focused aperture. The actual F-numbers, unlike the given F-number $F(f)$, cannot be defined by the user and vary not only with the frequency f but also with the focus $\mathbf{r}_\mathrm{f}$. The lateral focal coordinate x_f, as shown in Fig. 1, splits the interval $[x_\mathrm{l}; x_\mathrm{r}]$, which contains the aperture, into a left part $[x_\mathrm{l}; x_\mathrm{f})$ of width $A_\mathrm{l}/2 = x_\mathrm{f} - x_\mathrm{l}$ and a right part $[x_\mathrm{f}; x_\mathrm{r}]$ of width $A_\mathrm{r}/2 = x_\mathrm{r} - x_\mathrm{f}$. The actual F-numbers F_l and F_r divide the focal length z_f by the widths A_l and A_r, respectively, and equal

$$F_\mathrm{l} = \frac{z_\mathrm{f}}{A_\mathrm{l}} = \frac{z_\mathrm{f}}{2(x_\mathrm{f} - x_\mathrm{l})} \quad \text{and} \quad F_\mathrm{r} = \frac{z_\mathrm{f}}{A_\mathrm{r}} = \frac{z_\mathrm{f}}{2(x_\mathrm{r} - x_\mathrm{f})}. \tag{10}$$

These F-numbers, in the presence of aperture errors, differ from each other or from the given F-number $F(f)$. These differences, for the typical values of the given F-number (i.e., $F(f) \in [0.75; 2]$, see Section I), are insignificant for foci $\mathbf{r}_\mathrm{f}$ in the center of the FOV but increase in significance as the foci $\mathbf{r}_\mathrm{f}$ move to the lateral bounds of the FOV. Such foci cause asymmetric apertures in which one part is truncated by an edge of the linear array and, thus, narrower than the other part (e.g., $A_\mathrm{l} \gg A_\mathrm{r}$, see Fig. 1). One of the actual F-numbers (10), then, exceeds the given F-number $F(f)$ by multiples. The aperture errors, for small values of the given F-number (i.e., $F(f) \ll 0.75$), are always significant because the desired aperture width $A(z_\mathrm{f}, f)$ exceeds the width of the array (i.e., $A(z_\mathrm{f}, f) \gg (N_\mathrm{e} - 1)p_\mathrm{e} + w_\mathrm{e}$). Such small values of the given F-number $F(f)$ will arise for low frequencies.

2) Apodization: The apodization reduces sidelobe artifacts, which are caused by the aperture edges, at the expense of the lateral resolution [14, Sec. 7.2.9]. The required weights $\bar{a}_m(\mathbf{r}_\mathrm{f}, f)$, which will now be proposed, provide two advantages over the apodization weights in the literature [1], [3, eq. (2)], [6, eq. (15)], [13, eq. (30)] or software packages [26]. First, a reduction of sidelobe artifacts is ensured even in the presence of aperture errors (i.e., for foci $\mathbf{r}_\mathrm{f}$ near the lateral bounds of the FOV or small values of the given F-number $F(f)$, see Section II-A1). This advantage results from a window function $w(x)$ that is maximal near the lateral focal coordinate x_f and decreases gradually to zero near both lateral aperture bounds (9). This function accounts for asymmetric apertures by joining two window functions $w_\mathrm{l}(x)$ and $w_\mathrm{r}(x)$ at the lateral focal coordinate x_f and reads

$$w(x) = \begin{cases} 0, & \text{for } x \leq x_\mathrm{l} \text{ or } x \geq x_\mathrm{r} \\ w_\mathrm{l}(x), & \text{for } x_\mathrm{l} < x < x_\mathrm{f} \\ w_\mathrm{r}(x), & \text{for } x_\mathrm{f} \leq x < x_\mathrm{r}. \end{cases} \tag{11a}$$

The window functions $w_\mathrm{l}(x)$ and $w_\mathrm{r}(x)$ are centered on the lateral focal coordinate x_f and have the widths A_l and A_r, respectively. Suitable examples are the Hann windows $w_\mathrm{l}(x) = (1 + \cos[2\pi(x - x_\mathrm{f})/A_\mathrm{l}])/2$ and $w_\mathrm{r}(x) = (1 + \cos[2\pi(x - x_\mathrm{f})/A_\mathrm{r}])/2$. Second, the uniformity of the image intensity is improved, and the apodization-induced loss in the lateral resolution is reduced. This advantage results from a normalization of the proposed weights (i.e., $\sum_{m=0}^{N_\mathrm{e}-1} \bar{a}_m(\mathbf{r}_\mathrm{f}, f) = 1$) that read

$$\bar{a}_m(\mathbf{r}_\mathrm{f}, f) = \frac{w(x_{\mathrm{e},m})}{\sum_{m=0}^{N_\mathrm{e}-1} w(x_{\mathrm{e},m})} \tag{11b}$$

where $w(x_{\mathrm{e},m})$ are samples of the window function (11a) at the lateral center coordinates $x_{\mathrm{e},m}$ of the array elements defined in (3). The normalization scales the Fourier coefficients of the focused RF signal (6) as a function of both the focus $\mathbf{r}_\mathrm{f}$ and the frequency f. This scaling compensates the effect of any differences in the aperture width (i.e., the number of nonzero summands) on the moduli of the coefficients (6). The scaling, in particular, prevents an overweighting of low-frequency coefficients (6) relative to high-frequency coefficients (6). Low frequencies permit wider apertures than high frequencies and, thus, lead to more nonzero summands [see, e.g., Fig. 4(b), (c), and (g)].

3) Arrival Times: The focusing requires the arrival times $\Delta t_m(\mathbf{r}_\mathrm{f})$ of the spherical wave, which emanates from the image voxel at the focus $\mathbf{r}_\mathrm{f}$ upon insonification by the transmitted PW, at the individual array elements. These times will now be estimated using the average speed of sound $\bar{c}$ in the FOV and geometric distances. The required distances are the transmit distance $d^{(\mathrm{tx})}(\mathbf{r}_\mathrm{f})$, which the transmitted PW travels from the linear array to the focus $\mathbf{r}_\mathrm{f}$, and the receive distances $d_m^{(\mathrm{rx})}(\mathbf{r}_\mathrm{f})$, which the induced spherical wave travels

[1] An F-number of zero (i.e., $F(f) = 0$), herein, denotes the usage of the full aperture (i.e., $\mathbb{A}(\mathbf{r}_\mathrm{f}, f) = \mathbb{M}$) for all foci $\mathbf{r}_\mathrm{f}$.

from the focus $\mathbf{r}_\mathrm{f}$ to the centers of the individual array elements. The transmit distance $d^{(\mathrm{tx})}(\mathbf{r}_\mathrm{f})$, for a PW with the steering angle $\vartheta \in (-\pi/2; \pi/2)$ and the propagation direction $\mathbf{e}_\vartheta = (-\sin(\vartheta), 0, \cos(\vartheta))^\mathrm{T}$, amounts to [3, eq. (4)], [19, eq. (10.12)]

$$d^{(\mathrm{tx})}(\mathbf{r}_\mathrm{f}) = \cos(\vartheta) z_\mathrm{f} - \sin(\vartheta)(x_\mathrm{f} - x_\mathrm{ref}) \tag{12a}$$

where the lateral reference position $x_\mathrm{ref} = \mathrm{sgn}(\vartheta) M_\mathrm{e} p_\mathrm{e}$ with the sign function sgn ensures nonnegative distances. The receive distances $d_m^{(\mathrm{rx})}(\mathbf{r}_\mathrm{f})$, in contrast, are [3, eq. (5)], [19, eq. (10.9)]

$$d_m^{(\mathrm{rx})}(\mathbf{r}_\mathrm{f}) = \sqrt{(x_{\mathrm{e},m} - x_\mathrm{f})^2 + z_\mathrm{f}^2}. \tag{12b}$$

The arrival times $\Delta t_m(\mathbf{r}_\mathrm{f})$, dividing the sum of the distances (12a) and (12b) by the average speed of sound $\bar{c}$ in the FOV, become [3, eq. (6)], [6, eq. (2)]

$$\Delta t_m(\mathbf{r}_\mathrm{f}) = \frac{1}{\bar{c}}\left[d^{(\mathrm{tx})}(\mathbf{r}_\mathrm{f}) + d_m^{(\mathrm{rx})}(\mathbf{r}_\mathrm{f})\right]. \tag{12c}$$

4) Minimum Focal Length: The usage of the dynamic aperture (see Section II-A1) requires the focal length z_f to exceed a lower bound $z_\mathrm{f,lb}$ (i.e., $z_\mathrm{f} > z_\mathrm{f,lb}$) [13]. The focusing, in fact, can reduce the lateral beamwidth and, thus, improve the lateral resolution only if the aperture is wide enough to ensure near-field operation. Near-field operation requires the near-field distance z_NF of the unfocused aperture to exceed the focal length z_f (i.e., $z_\mathrm{NF} > z_\mathrm{f}$) [14, p. 173], [15], [19, pp. 190–191], [20]. The near-field distance z_NF, using a rectangular piston with the width $A(z_\mathrm{f}, f) = z_\mathrm{f}/F(f)$ to approximate the unfocused aperture, amounts to $z_\mathrm{NF} \approx A^2(z_\mathrm{f}, f)/(2.88\lambda)$ [27] and increases quadratically with the focal length z_f. The focal length z_f, hence, must exceed the lower bound

$$z_\mathrm{f,lb} \approx 2.88\lambda F^2(f). \tag{13}$$

This constraint (i.e., $z_\mathrm{f} > z_\mathrm{f,lb}$), conversely, limits the F-number $F(f)$ for any given focal length z_f.

B. Far-Field Directivity Pattern of the Focused Aperture

The effects of the actual F-numbers (10) and the frequency on the far-field directivity pattern of the focused aperture will now be discussed. These effects explain the tradeoff between the reduction of grating lobe artifacts and the improvement of the lateral resolution (see Section I) and will be used in Section II-C to derive the proposed F-number. The far-field directivity pattern, as shown in Appendix A, quantifies the sensitivity of the Fourier coefficients of the focused RF signal (6) to incoming PWs. Each PW propagates parallel to the image plane in a specific direction $\mathbf{e}_\alpha = (\sin(\alpha), 0, -\cos(\alpha))^\mathrm{T}$, where $\alpha \in (-\pi/2; \pi/2)$ denotes the arrival angle with respect to the z-axis, and has a specific normalized lateral frequency $\bar{k}_x = \sin(\alpha)$. The far-field directivity pattern $S(\bar{k}_x)$ is a function of this frequency $\bar{k}_x$ and, as shown in Appendix B-A, superimposes a main lobe $S_0(\bar{k}_x)$ and infinitely many grating lobes $S_l(\bar{k}_x)$ of the order $l \in \mathbb{Z} \setminus \{0\}$, i.e.,

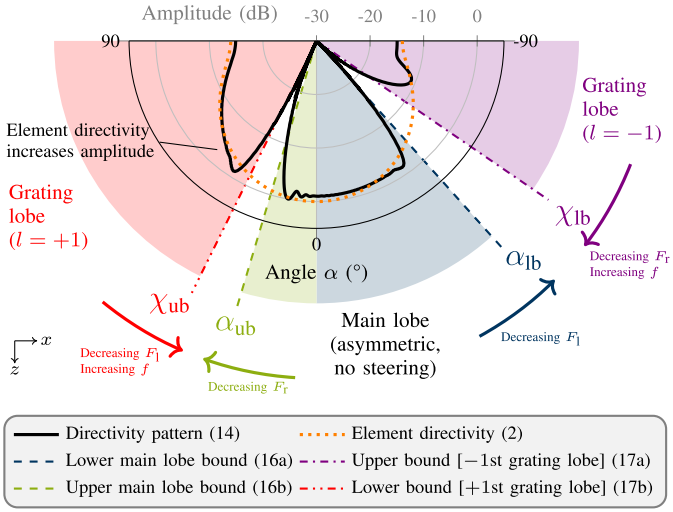

Fig. 2. Effects of the actual F-numbers (10) and the frequency f on the far-field directivity pattern (14). This pattern, which is shown for $F_\mathrm{l} \approx 0.56$, $F_\mathrm{r} \approx 1.67$, $\bar{p}_\mathrm{e} = 0.9$, and the parameters given in Section IV-A, describes the sensitivity of the focused aperture to incoming plane waves. These waves propagate parallel to the image plane and arrive at the aperture at the angle $\alpha = \arcsin(\bar{k}_x)$ for $|\bar{k}_x| < 1$. The pattern superimposes a desired main lobe and undesired grating lobes. The angular bounds of the main lobe (16) increase in modulus with decreasing F-numbers (10) but are independent of the frequency f. The angular distances of the first-order grating lobes (17), in contrast, decrease in modulus with decreasing F-numbers (10) and increasing frequency f. These distances, due to the element directivity (2), determine the grating lobe amplitudes. The asymmetry of the main lobe (i.e., $|\alpha_\mathrm{lb}| > \alpha_\mathrm{ub}$) results from different widths of the left and right parts of the aperture (i.e., $F_\mathrm{l} \ll F_\mathrm{r}$, see Fig. 1) and not beam steering.

$$S(\bar{k}_x) \propto S_0(\bar{k}_x) + \sum_{|l|=1}^{\infty} S_l(\bar{k}_x) \tag{14a}$$

where $\propto$ is proportionality. Each lobe $S_l(\bar{k}_x)$ multiplies a shifted copy $H(\bar{k}_x - l\bar{k}_\mathrm{s})$ of a single Fourier transform $H(\bar{k}_x)$ by a sinc function and reads

$$S_l(\bar{k}_x) = \tau_l \,\mathrm{sinc}\left(\bar{k}_x \frac{w_\mathrm{e}}{\lambda}\right) H(\bar{k}_x - l\bar{k}_\mathrm{s}) \tag{14b}$$

where $\tau_l = (-1)^{l(N_\mathrm{e}-1)}/p_\mathrm{e}$ are weights and $\bar{k}_\mathrm{s} = \lambda/p_\mathrm{e} = 1/\bar{p}_\mathrm{e}$ is the normalized lateral sampling frequency with the normalized element pitch $\bar{p}_\mathrm{e} = p_\mathrm{e}/\lambda$. The Fourier transform $H(\bar{k}_x)$, which lacks a closed form, describes the far-field directivity pattern of a continuous version of the aperture. The shifted copies $H(\bar{k}_x - l\bar{k}_\mathrm{s})$ result from the discretization of this continuous aperture by the equispaced elements of the linear array. The sinc function reflects the element directivity (2) and decreases the modulus of the pattern (14) with increasing lateral frequency $|\bar{k}_x|$. Two important properties of all lobes (14b), however, justify an exclusive consideration of the main lobe $S_0(\bar{k}_x)$ and the first-order grating lobes $S_{\pm1}(\bar{k}_x)$.

First, each lobe (14b) has specific lateral band limits (i.e., there are lower and upper bounds $\bar{k}_{x,\mathrm{lb}}^{(l)}$ and $\bar{k}_{x,\mathrm{ub}}^{(l)} > \bar{k}_{x,\mathrm{lb}}^{(l)}$, respectively, such that $|S_l(\bar{k}_x)| \approx 0$ for $\bar{k}_x < \bar{k}_{x,\mathrm{lb}}^{(l)}$ or $\bar{k}_x > \bar{k}_{x,\mathrm{ub}}^{(l)}$). These band limits, which will be called "lobe bounds," result from shifting the main lobe bounds $\bar{k}_{x,\mathrm{lb}} \in (-1; 0)$ and

$\bar{k}_{x,\mathrm{ub}} \in (0; 1)$ by an integer multiple l of the normalized lateral sampling frequency $\bar{k}_\mathrm{s}$ and read

$$\bar{k}_{x,\mathrm{lb}}^{(l)} = l\bar{k}_\mathrm{s} + \bar{k}_{x,\mathrm{lb}} \tag{15a}$$

$$\bar{k}_{x,\mathrm{ub}}^{(l)} = l\bar{k}_\mathrm{s} + \bar{k}_{x,\mathrm{ub}}. \tag{15b}$$

The main lobe bounds $\bar{k}_{x,\mathrm{lb}}$ and $\bar{k}_{x,\mathrm{ub}}$, as shown in Appendix B-B, derive from an approximation of the Fourier transform $H(\bar{k}_x)$ and only depend on the actual F-numbers (10). The shift $|l\bar{k}_\mathrm{s}|$, in contrast, increases with increasing order $|l|$ and, due to the identity $\bar{k}_\mathrm{s} = \bar{c}/(p_\mathrm{e} f)$, decreasing frequency f. Only those lobes (14b) that lie in the lateral frequency band associated with propagable PWs (i.e., $|\bar{k}_x| < 1$), however, are relevant. Such lobes define angular sectors within which incoming PWs can be detected and, in the near field, represent receive beams. The main lobe $S_0(\bar{k}_x)$ is always relevant (i.e., $-1 < \bar{k}_{x,\mathrm{lb}} < \bar{k}_{x,\mathrm{ub}} < 1$) and represents the desired receive beam. The first-order grating lobes $S_{\pm1}(\bar{k}_x)$, which occur next to the main lobe $S_0(\bar{k}_x)$, become relevant before higher order grating lobes (i.e., $|l| > 1$) and, then, represent undesired receive beams that can cause interference.

Second, the lobes (14b) decrease in modulus with increasing order $|l|$. This decrease results from the fact that the Fourier transform $H(\bar{k}_x)$ acts as a window function (i.e., $|H(\bar{k}_x)| \approx 0$ for $\bar{k}_x < \bar{k}_{x,\mathrm{lb}}$ or $\bar{k}_x > \bar{k}_{x,\mathrm{ub}}$, see Appendix B-B) whose shifted copies $H(\bar{k}_x - l\bar{k}_\mathrm{s})$ segment the sinc function. The segments have the bounds (15) and, due to the decay of the sinc function with increasing lateral frequency $|\bar{k}_x|$, decrease in modulus as the order $|l|$ increases. The main lobe $S_0(\bar{k}_x)$ and the first-order grating lobes $S_{\pm1}(\bar{k}_x)$, thus, can attain higher amplitudes than higher order grating lobes (i.e., $|l| > 1$), and the associated receive beams can cause the strongest interference. The amplitudes of the lobes $S_0(\bar{k}_x)$ and $S_{\pm1}(\bar{k}_x)$ vary with the associated bounds (15). The dependence of these bounds on the actual F-numbers (10) and the frequency f will now be analyzed to describe the interference due to the limited lateral resolution and the grating lobes.

1) Main Lobe Bounds: The main lobe $S_0(\bar{k}_x)$ is low-pass band-limited (i.e., $|S_0(\bar{k}_x)| \approx 0$ for $\bar{k}_x < \bar{k}_{x,\mathrm{lb}}$ or $\bar{k}_x > \bar{k}_{x,\mathrm{ub}}$). The lower and upper bounds $\bar{k}_{x,\mathrm{lb}}$ and $\bar{k}_{x,\mathrm{ub}}$, as shown in Appendix B-B, only depend on the actual F-numbers (10) of the left and right parts of the aperture, respectively. These dependencies read

$$\sin(\alpha_\mathrm{lb}) = \bar{k}_{x,\mathrm{lb}} = -\frac{1}{\sqrt{1 + (2F_\mathrm{l})^2}} \tag{16a}$$

$$\sin(\alpha_\mathrm{ub}) = \bar{k}_{x,\mathrm{ub}} = \frac{1}{\sqrt{1 + (2F_\mathrm{r})^2}} \tag{16b}$$

where $\alpha_\mathrm{lb} \in (-\pi/2; 0)$ and $\alpha_\mathrm{ub} \in (0; \pi/2)$ denote the lower and upper angular bounds of the main lobe, respectively. The angular bounds (16), as shown in Fig. 2, increase in modulus with decreasing F-numbers (10). This increase can be explained by a simple model of the desired receive beam. This model, as shown in Fig. 1, consists of two rays that start at the aperture edges in the image plane and intersect at the focus. The resulting angular aperture, due to basic trigonometric relations, has the bounds (16) and, thus, equals the angular sector within which the main lobe can detect incoming PWs.

2) First-Order Grating Lobe Bounds: The first-order grating lobes $S_{\pm1}(\bar{k}_x)$ are bandpass band-limited (i.e., $|S_l(\bar{k}_x)| \approx 0$ for $\bar{k}_x < l\bar{k}_\mathrm{s} + \bar{k}_{x,\mathrm{lb}}$ or $\bar{k}_x > l\bar{k}_\mathrm{s} + \bar{k}_{x,\mathrm{ub}}$ with $l = \pm1$). These lobes, considering the identity $\bar{k}_\mathrm{s} = 1/\bar{p}_\mathrm{e}$ and the main lobe bounds (16), are relevant only if the element pitch p_e violates the sampling theorem (i.e., $\bar{p}_\mathrm{e} > 0.5$) and the actual F-numbers (10) are sufficiently small. The upper bound $\bar{k}_{x,\mathrm{ub}}^{(-1)} = -\bar{k}_\mathrm{s} + \bar{k}_{x,\mathrm{ub}}$ of the -1st grating lobe $S_{-1}(\bar{k}_x)$ and the lower bound $\bar{k}_{x,\mathrm{lb}}^{(1)} = \bar{k}_\mathrm{s} + \bar{k}_{x,\mathrm{lb}}$ of the $+1$st grating lobe $S_1(\bar{k}_x)$ then define signed angular distances $\chi_\mathrm{lb} \in (-\pi/2; \pi/2)$ and $\chi_\mathrm{ub} \in (-\pi/2; \pi/2)$, respectively. These distances meet

$$\sin(\chi_\mathrm{lb}) = -\bar{k}_\mathrm{s} + \bar{k}_{x,\mathrm{ub}} = -\frac{1}{\bar{p}_\mathrm{e}} + \frac{1}{\sqrt{1 + (2F_\mathrm{r})^2}} \tag{17a}$$

$$\sin(\chi_\mathrm{ub}) = \bar{k}_\mathrm{s} + \bar{k}_{x,\mathrm{lb}} = \frac{1}{\bar{p}_\mathrm{e}} - \frac{1}{\sqrt{1 + (2F_\mathrm{l})^2}} \tag{17b}$$

and show that the main lobe $S_0(\bar{k}_x)$ and the first-order grating lobes $S_{\pm1}(\bar{k}_x)$ can overlap (i.e., occupy the same angles). Such overlaps, as will be argued in Section II-B3, distort the desired receive beam and, thus, will be eliminated by defining a suitable F-number. All the following discussions, hence, apply to the interesting case in which lobe overlaps are absent and the angular distances (17) satisfy $\chi_\mathrm{lb} < \alpha_\mathrm{lb}$ and $\chi_\mathrm{ub} > \alpha_\mathrm{ub}$. In this case, which is shown in Fig. 2, the angular distances (17) decrease in modulus with: 1) decreasing F-numbers (10) and 2) due to the inverse proportionality $\bar{k}_\mathrm{s} \propto 1/f$, increasing frequency. The sinc function, which reflects the element directivity (2) in the lobes (14b), thereby increases the grating lobe amplitudes. This increase results in a tradeoff between the reduction of grating lobe artifacts and the improvement of the lateral resolution. Any such improvement requires wider apertures or, equivalently, smaller F-numbers (10). Such F-numbers, however, decrease the grating lobe distances (17) in modulus and, thus, increase the grating lobe amplitudes.

3) Lobe Aliasing: Overlaps between the main and grating lobes, due to the superposition (14a) of all lobes (14b), distort the desired receive beam and, thus, must be avoided. Such overlaps occur if the main lobe bounds (16) exceed the grating lobe distances (17) (i.e., $\alpha_\mathrm{lb} < \chi_\mathrm{lb}$ or $\alpha_\mathrm{ub} > \chi_\mathrm{ub}$). The overlaps, to the best knowledge of the authors, have never been reported in the literature and, according to the aliasing effect in undersampled signals, will be called "lobe aliasing." The avoidance of lobe aliasing is a new method that is proposed herein and will be called "lobe antialiasing." This method increases the given F-number $F(f)$ and, thus, the actual F-numbers (10) with the frequency. The resulting reduction in the moduli of the main lobe bounds (16) compensates the effect of the normalized lateral sampling frequency $\bar{k}_\mathrm{s}$. This frequency $\bar{k}_\mathrm{s}$, as explained in Section II-B2 and shown in Fig. 2, reduces the grating lobe distances (17) in modulus with increasing frequency f. Let the angle $\delta \in [0, \pi/2)$ denote a safety margin that accounts for any approximation errors in the main (16) and grating lobe bounds (17). The lobe antialiasing conditions $\chi_\mathrm{lb} < \alpha_\mathrm{lb} - \delta$ and $\chi_\mathrm{ub} > \alpha_\mathrm{ub} + \delta$ then yield

$$\frac{\cos(\delta) + 2F_\mathrm{l}\sin(\delta)}{\sqrt{1 + (2F_\mathrm{l})^2}} + \frac{1}{\sqrt{1 + (2F_\mathrm{r})^2}} < \frac{1}{\bar{p}_\mathrm{e}} \tag{18a}$$

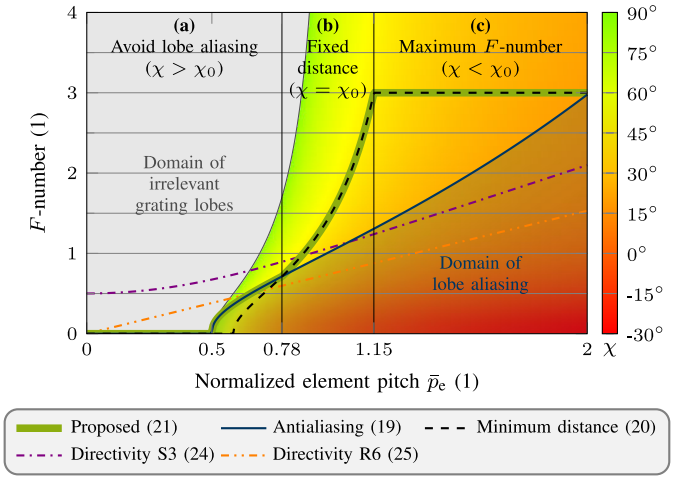

Fig. 3. Effect of the proposed *F*-number (21) on the angular distances of the first-order grating lobes (17). Both distances, if the aperture is error-free [i.e., $F_\mathrm{l} = F_\mathrm{r} = F(\bar{p}_\mathrm{e})$], are equal (i.e., $\chi_\mathrm{ub} = -\chi_\mathrm{lb} = \chi$) and exclusively depend on the frequency and the given *F*-number $F(\bar{p}_\mathrm{e})$. The proposed *F*-number (21), which is shown for $\chi_0 = 45°$, $F_\mathrm{ub} = 3$, and $\delta = 10°$, maximizes the lateral resolution under two constraints. This *F*-number, for (a) low frequencies (i.e., $\bar{p}_\mathrm{e} \leq 0.78$), equals the lower bound (19) to avoid lobe aliasing. The grating lobes, in this frequency range, are either irrelevant or their angular distances (17) exceed the given minimum (i.e., $\chi > \chi_0$). The proposed *F*-number (21), for higher frequencies (i.e., $\bar{p}_\mathrm{e} > 0.78$), equals the lower bound (20). This bound, around (b) center frequency (i.e., $0.78 < \bar{p}_\mathrm{e} < \bar{p}_\mathrm{e,ub} \approx 1.15$), fixes the angular distances (17) and, thus, limits the grating lobe amplitudes. This bound, for (c) high frequencies (i.e., $\bar{p}_\mathrm{e} \geq \bar{p}_\mathrm{e,ub}$), equals the maximum permissible *F*-number (i.e., $F(\bar{p}_\mathrm{e}) = F_\mathrm{ub}$) to sustain the focusing. The directivity-derived *F*-numbers (24) and (25), which will be introduced in Section IV-D2 and are shown for $w_\mathrm{e}/p_\mathrm{e} = 91.8\%$, do not control the grating lobes and serve as references.

$$\frac{\cos(\delta) + 2F_\mathrm{r}\sin(\delta)}{\sqrt{1+(2F_\mathrm{r})^2}} + \frac{1}{\sqrt{1+(2F_\mathrm{l})^2}} < \frac{1}{\bar{p}_\mathrm{e}} \tag{18b}$$

where the inequalities $\sin(\chi_\mathrm{lb}) < \sin(\alpha_\mathrm{lb} - \delta)$ and $\sin(\chi_\mathrm{ub}) > \sin(\alpha_\mathrm{ub} + \delta)$ were expanded combining the sine addition theorems with the main (16) and grating lobe bounds (17).

C. Proposed F-Number

The proposed *F*-number will now be derived. The derivation will be simplified by replacing the frequency f as the independent variable by the normalized element pitch $\bar{p}_\mathrm{e} = p_\mathrm{e} f/\bar{c}$. The proposed *F*-number $\hat{F}(\bar{p}_\mathrm{e})$ maximizes the aperture width and, thus, the lateral resolution under two constraints. Each constraint, as will be shown, limits the GLL in a specific frequency range and imposes a lower bound on the given *F*-number $F(\bar{p}_\mathrm{e})$. The first constraint limits the GLL for low frequencies by avoiding lobe aliasing. This constraint is represented by the antialiasing conditions (18) and yields the lower bound $F_\mathrm{lb}^{(\mathrm{A})}(\bar{p}_\mathrm{e})$. The second constraint, in contrast, limits the GLL for higher frequencies by using the element directivity (2). This constraint imposes a lower bound on the moduli of the grating lobe distances (17) to reduce the grating lobe amplitudes (see Fig. 2) and yields the lower bound $F_\mathrm{lb}^{(\mathrm{G})}(\bar{p}_\mathrm{e})$. Both constraints, which the proposed *F*-number $\hat{F}(\bar{p}_\mathrm{e})$ meets by selecting the maximum of the associated lower bounds, define a minimum dynamic range available for unambiguous imaging.

The proposed *F*-number $\hat{F}(\bar{p}_\mathrm{e})$ must ensure that the above constraints hold in the presence of aperture errors. Such errors, which lead to significant deviations of the actual *F*-numbers (10) from the given *F*-number $F(\bar{p}_\mathrm{e})$ for foci $\mathbf{r}_\mathrm{f}$ near the lateral bounds of the FOV or small values of the given *F*-number $F(\bar{p}_\mathrm{e})$ (see Section II-A1), have to be factored into the apodization weights (11) and the far-field directivity pattern (14). The following derivations, however, may be simplified by assuming an error-free aperture [i.e., $F_\mathrm{l} = F_\mathrm{r} = F(\bar{p}_\mathrm{e})$] because there are only two kinds of aperture errors, and neither kind affects the lower bounds $F_\mathrm{lb}^{(\mathrm{A})}(\bar{p}_\mathrm{e})$ and $F_\mathrm{lb}^{(\mathrm{G})}(\bar{p}_\mathrm{e})$. First, the lateral bounds (9) can exceed the desired bounds $x_\mathrm{f} \pm A(z_\mathrm{f}, \bar{p}_\mathrm{e})/2$. Any such exceedance, however, is limited by half the element width $w_\mathrm{e}/2$ (i.e., $x_\mathrm{l} \geq x_\mathrm{f} - [A(z_\mathrm{f}, \bar{p}_\mathrm{e}) + w_\mathrm{e}]/2$ and $x_\mathrm{r} \leq x_\mathrm{f} + [A(z_\mathrm{f}, \bar{p}_\mathrm{e}) + w_\mathrm{e}]/2$). This error is negligible for the usual focal lengths z_f [i.e., $F_\mathrm{l}, F_\mathrm{r} \geq F(\bar{p}_\mathrm{e})$ for $z_\mathrm{f} \gg w_\mathrm{e} F(\bar{p}_\mathrm{e})$]. Second, the lateral bounds (9) can fall below the desired bounds. Such apertures, however, meet the above constraints if the error-free aperture obeys them. The constraints hold more easily for large actual *F*-numbers (10) (see Fig. 2), and at least one actual *F*-number (10) exceeds the given *F*-number (e.g., $F_\mathrm{r} \gg F_\mathrm{l} \approx F(\bar{p}_\mathrm{e})$, see Fig. 1).

1) Lobe Antialiasing Constraint: The antialiasing conditions (18), considering an error-free aperture [i.e., $F_\mathrm{l} = F_\mathrm{r} = F(\bar{p}_\mathrm{e})$] and assuming a small safety margin (i.e., $\delta \ll 1$), yield the lower bound on the *F*-number

$$F_\mathrm{lb}^{(\mathrm{A})}(\bar{p}_\mathrm{e}) = \begin{cases} 0, & \text{for } \bar{p}_\mathrm{e} < 0.5 \\ \dfrac{\sqrt{\bar{p}_\mathrm{e}^{\,2} - 0.25} + \bar{p}_\mathrm{e}^{\,2}\delta}{1 - \bar{p}_\mathrm{e}^{\,2}\delta^2}, & \text{for } 0.5 \leq \bar{p}_\mathrm{e} < 1/\delta \end{cases} \tag{19}$$

where the safety margin justified the approximations $\sin(\delta) \approx \delta$ and $\cos(\delta) \approx 1$. This bound, as shown in Fig. 3 for $\delta = 10°$, permits the usage of the full aperture (i.e., $F_\mathrm{lb}^{(\mathrm{A})}(\bar{p}_\mathrm{e}) = 0$) if the grating lobes are irrelevant (i.e., $\bar{p}_\mathrm{e} < 0.5$). The bound then increases from a value of approximately zero at $\bar{p}_\mathrm{e} = 0.5$ to a value of approximately three at $\bar{p}_\mathrm{e} = 2$. The grating lobe distances (17) decrease from $\chi_\mathrm{ub} = -\chi_\mathrm{lb} = \chi \approx 90°$ at $\bar{p}_\mathrm{e} = 0.5$ to $\chi \approx 20°$ at $\bar{p}_\mathrm{e} = 2$ and amount to only $\chi \approx 35°$ near the center frequency (i.e., $\bar{p}_\mathrm{e} \approx 1$). Small distances in the spectral center, however, permit strong interference because the element directivity (2), as shown in Fig. 2, increases the grating lobe amplitudes with decreasing distances.

2) Minimum Angular Distance Constraint: The imposition of a minimum angular distance $\chi_0 \in (0; \pi/2]$ on the first-order grating lobes, due to the element directivity (2), limits their amplitudes. This limitation, however, requires frequencies below a cutoff. This cutoff derives from a maximum permissible *F*-number $F_\mathrm{ub} > 0$ that avoids very narrow apertures. Such apertures cannot reduce the lateral beamwidth and render the focusing ineffective (see Section II-A4). The grating lobe distances (17), considering an error-free aperture [i.e., $F_\mathrm{l} = F_\mathrm{r} = F(\bar{p}_\mathrm{e})$], noticing equal distances (i.e., $\chi_\mathrm{ub} = -\chi_\mathrm{lb} = \chi$), and imposing the given minimum [i.e., $\sin(\chi) > \sin(\chi_0)$],

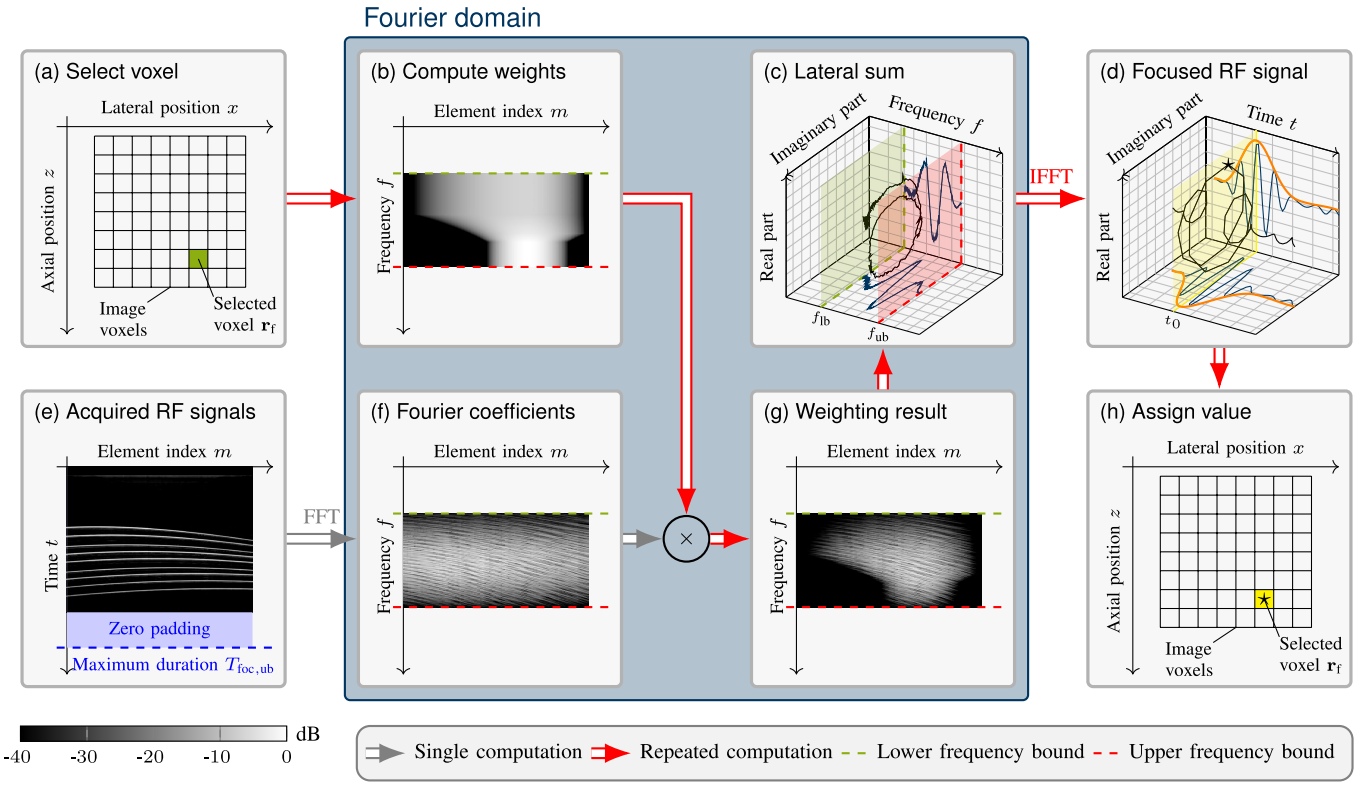

Fig. 4. Proposed Fourier-domain beamforming algorithm. Inputs include (a) grid of voxels and (e) digitized RF signals. The algorithm first computes (f) Fourier coefficients of the acquired RF signals (5) by a zero-padded FFT and then separately processes all image voxels. For any selected voxel and each frequency, the receive aperture derives from (b) complex-valued apodization weights (7). The multiplication of these weights by (f) Fourier coefficients of the acquired RF signals (5) yields (g) weighted coefficients and, upon lateral summation, (c) Fourier coefficients of the focused RF signal (6). An inverse fast Fourier transform (IFFT) provides (d) focused RF signal (4). A specific sample of this signal yields (h) complex voxel value (22). The steps [see (c) and (d)] can be summarized in a 2-D sum of (g) weighted coefficients if (b) complex-valued apodization weights (7) are replaced by $w_m(\mathbf{r}_\mathrm{f}, f)e^{j2\pi f t_0}$.

yield the lower bound on the F-number

$$F_\mathrm{lb}^{(\mathrm{G})}(\bar{p}_\mathrm{e}) = \begin{cases} 0, & \text{for } \bar{p}_\mathrm{e} \le \bar{p}_\mathrm{e,lb} \\ \dfrac{1}{2}\sqrt{\dfrac{1}{\left[1/\bar{p}_\mathrm{e} - \sin(\chi_0)\right]^2} - 1}, & \text{for } \bar{p}_\mathrm{e} \in \mathbb{P} \\ F_\mathrm{ub}, & \text{for } \bar{p}_\mathrm{e} \ge \bar{p}_\mathrm{e,ub} \end{cases} \tag{20a}$$

where $\mathbb{P} = (\bar{p}_\mathrm{e,lb}; \bar{p}_\mathrm{e,ub})$ and the lower and upper bounds on the normalized element pitch are

$$\bar{p}_\mathrm{e,lb} = \frac{1}{\sin(\chi_0) + 1} \tag{20b}$$

$$\bar{p}_\mathrm{e,ub} = \frac{1}{\sin(\chi_0) + \frac{1}{\sqrt{1+(2F_\mathrm{ub})^2}}}. \tag{20c}$$

This bound, as shown in Fig. 3 for $\chi_0 = 45°$ and $F_\mathrm{ub} = 3$, permits the usage of the full aperture (i.e., $F_\mathrm{lb}^{(\mathrm{G})}(\bar{p}_\mathrm{e}) = 0$) if the grating lobes are irrelevant or their distances exceed the minimum (i.e., $\bar{p}_\mathrm{e} \le \bar{p}_\mathrm{e,lb} \approx 0.59$). The bound then increases steeply from the value of zero at $\bar{p}_\mathrm{e} = \bar{p}_\mathrm{e,lb}$ to the maximum permissible F-number at $\bar{p}_\mathrm{e} = \bar{p}_\mathrm{e,ub} \approx 1.15$. The grating lobe distances (17) thereby equal the given minimum (i.e., $\chi = \chi_0$). The bound equals the maximum permissible F-number (i.e., $F_\mathrm{lb}^{(\mathrm{G})}(\bar{p}_\mathrm{e}) = F_\mathrm{ub}$) for $\bar{p}_\mathrm{e} \ge \bar{p}_\mathrm{e,ub}$ to sustain the focusing. The lower bound (20), however, falls below the antialiasing bound (19) for $0.5 \le \bar{p}_\mathrm{e} < 0.78$ and, thus, permits lobe aliasing.

3) Proposition: The proposed F-number $\hat{F}(\bar{p}_\mathrm{e})$ equals the maximum of the lower bounds (19) and (20) to avoid lobe aliasing and impose a minimum distance on the first-order grating lobes. The proposed F-number $\hat{F}(\bar{p}_\mathrm{e})$, thus, reads

$$\hat{F}(\bar{p}_\mathrm{e}) = \max\left\{F_\mathrm{lb}^{(\mathrm{A})}(\bar{p}_\mathrm{e}), F_\mathrm{lb}^{(\mathrm{G})}(\bar{p}_\mathrm{e})\right\} \tag{21}$$

for $\bar{p}_\mathrm{e} < 1/\delta$. This F-number, as shown in Fig. 3 for $\chi_0 = 45°$, $F_\mathrm{ub} = 3$, and $\delta = 10°$, avoids lobe aliasing for $\bar{p}_\mathrm{e} \le 0.78$. It fixes the grating lobe distances (17) for $0.78 < \bar{p}_\mathrm{e} < \bar{p}_\mathrm{e,ub} \approx 1.15$ and sustains the focusing for $\bar{p}_\mathrm{e} \ge \bar{p}_\mathrm{e,ub}$. Note that larger F-numbers [i.e., $F(\bar{p}_\mathrm{e}) > \hat{F}(\bar{p}_\mathrm{e})$] also meet both lower bounds. Such F-numbers, however, narrow the aperture and, thus, reduce the lateral resolution.

III. Implementation

The algorithm, which implemented the image formation in the Fourier domain, will now be described. This algorithm, as shown in Fig. 4, determined the echogenicity of each image voxel by estimating the echoed pulse (see Section II-A) and measuring its amplitude. The value $I(\mathbf{r}_\mathrm{f})$ of the voxel at the focus $\mathbf{r}_\mathrm{f}$, as shown in Fig. 4(d) and (h), equaled the focused RF signal (4) at a given time t_0, i.e.,

$$I(\mathbf{r}_\mathrm{f}) \approx \sum_{\nu=\nu_\mathrm{lb}}^{\nu_\mathrm{ub}} \sum_{m=0}^{N_\mathrm{e}-1} w_m(\mathbf{r}_\mathrm{f}, f_\nu) e^{j2\pi f_\nu t_0} U_m(f_\nu). \tag{22}$$

The time t_0 depended on the electromechanical pulse-echo response and, as shown in Fig. 4(d), equaled the time of the maximum envelope. The Fourier coefficients of the acquired RF signals (5), as shown in Fig. 4(e) and (f), were computed from digitized versions of the acquired RF signals $u_m(t)$ using zero-padded fast Fourier transforms (FFTs) [24, Sec. 2.4.]. The zero padding prevented aliasing in the focused RF signal (4) by accounting for its maximum time duration $T_{\mathrm{foc,ub}}$ for all foci. This duration equaled the sum of the duration of the acquired RF signals $u_m(t)$ and the maximum difference in the arrival times (12) for any fixed focus and all array elements. The lower and upper frequency indices ν_{lb} and ν_{ub} amounted to $\nu_{\mathrm{lb}} = \lceil T_{\mathrm{foc,ub}} f_{\mathrm{lb}} \rceil$ and $\nu_{\mathrm{ub}} = \lfloor T_{\mathrm{foc,ub}} f_{\mathrm{ub}} \rfloor$, respectively, where f_{lb} and f_{ub} are the band limits of the acquired RF signals $u_m(t)$ (see Section II) and $\lceil \cdot \rceil$ and $\lfloor \cdot \rfloor$ are the ceiling and floor functions, respectively.

IV. Methods

Five experiments validated the proposed F-number (21). The first two experiments exposed the effect of the F-number on the receive beam in the focal plane. The remaining experiments showed the advantages of the proposed F-number (21) in the formation of B-mode images. The specifications of the linear array ($N_{\mathrm{e}} = 128$, $w_{\mathrm{e}} = 279.8$ μm, $h_{\mathrm{e}} = 4$ mm, and $p_{\mathrm{e}} = 304.8$ μm), in all experiments, were identical. The lower and upper frequency bounds were $f_{\mathrm{lb}} = 2.25$ MHz and $f_{\mathrm{ub}} = 6.75$ MHz, respectively. Dynamic receive apertures with the proposed F-number (21) and three additional F-numbers, which will be described in the end of this section, were compared to the full aperture (i.e., $F = 0$). The apodization weights (11) derived from Tukey windows with a cosine fraction of 20 %. MATLAB R2021a (The MathWorks, Inc., Natick, MA, USA) enabled all numerical calculations.

A. Receive Beam in the Focal Plane

The receive beam in the focal plane revealed the lateral width of the main lobe and the positions and the maximum amplitude of the grating lobes. All numerical calculations used the exact equations in Appendixes A and B-A. The far-field directivity pattern (31) was inserted into the inverse transverse Fourier transform (29a). The focus $\mathbf{r}_{\mathrm{f}}/p_{\mathrm{e}} = (32, 0, 107)^{\mathrm{T}}$ promoted asymmetric apertures (i.e., $A_{\mathrm{l}} \gg A_{\mathrm{r}}$, see Fig. 1 and Section II-A1). The normalized element pitch $\bar{p}_{\mathrm{e}}$, combining the frequency bounds with an average speed of sound $\bar{c} = 1540$ m/s and an absorption coefficient $\alpha/f = 0.5$ dB/MHz/cm, ranged from 0.45 to 1.34. The inverse transform (29a) was evaluated for voxel positions $\mathbf{r}_0 = (x_0, 0, z_{\mathrm{f}})^{\mathrm{T}}$, where the lateral distance $\Delta x = x_0 - x_{\mathrm{f}}$ ranged from -101 to 101 mm. The sampling period was a quarter of the minimum wavelength λ_{lb} and equaled $\lambda_{\mathrm{lb}}/4 \approx 57$ μm. The subtraction of the main lobe from the far-field directivity pattern (31), according to the Poisson summation formula (33), isolated the grating lobes. Their lower and upper lateral bounds $x_{\mathrm{g,lb}}$ and $x_{\mathrm{g,ub}}$ were estimated as

$$x_{\mathrm{g,lb}} = x_{\mathrm{f}} - z_{\mathrm{f}} \tan(\chi_{\mathrm{ub}}) \tag{23a}$$

$$x_{\mathrm{g,ub}} = x_{\mathrm{f}} - z_{\mathrm{f}} \tan(\chi_{\mathrm{lb}}). \tag{23b}$$

The lateral main lobe width at each frequency derived from the full-width at half-maximum (FWHM), and the maximum grating lobe amplitude was assessed by the GLL.

B. Parameter Sweeps

Four parameter sweeps revealed the effects of the given F-number $F(\bar{p}_{\mathrm{e}})$ and the minimum angular distance χ_0, which the proposed F-number (21) imposed on the first-order grating lobes, on the GLL of the receive beam in the focal plane. All sweeps, unless mentioned otherwise, used the parameters from Section IV-A. The first sweep covered all actual F-numbers (10) that the linear array allowed for the focus $\mathbf{r}_{\mathrm{f}}/p_{\mathrm{e}} = (63.5, 0, 44)^{\mathrm{T}}$. These F-numbers included values down to $F_{\mathrm{l}} \approx 0.17$, which cause severe grating lobes. Three additional sweeps used the results of the first sweep to cover the minimum angular distances χ_0 from 26° to 90° with a step size of 1°. The maximum permissible F-number, considering the minimum focal length (13) at the maximum wavelength $\lambda_{\mathrm{ub}} \approx 684$ μm, was $F_{\mathrm{ub}} = 2.6$, and the safety margins were $\delta \in \{0°, 10°\}$. The minimum angular distance bound (20) served as a reference to show the lobe antialiasing effect.

C. B-Mode Image Formation

B-mode images were formed to investigate their quality. A programmable UI system (SonixTouch Research, Analogic Corporation, Richmond, BC, Canada) with a linear array (model: L14-5/38) acquired and stored all RF channel data for offline processing (sampling rate: 40 MHz). Two phantoms, namely a wire and a tissue phantom, and the common carotid artery of a volunteer (in vivo) were scanned. Each scan used 11 steering angles between $-20°$ and 20° with a spacing of 4°. Only one scan per object was processed to ensure that all receive aperture types use the same RF data set and, thus, produce comparable images. Single PW images were formed using steering angles of 0° for the wire phantom and $-20°$ for both remaining objects. Both angles ensured an insonification of off-axis reflectors and, thus, promoted the emergence of grating lobe artifacts. Compound images were formed using three ($-16°$, 0°, 16°) and all 11 steering angles. The number of image voxels and their spacing on each axis amounted to 512 and $p_{\mathrm{e}}/4 = 76.2$ μm, respectively.

1) Phantoms: The wire phantom consisted of nine wires suspended in a tap water tank ($\bar{c} = 1470$ m/s). The axial wire distances from the linear array approximately ranged from 31.6 to 62.4 mm, and the mean axial and lateral spacings amounted to approximately 4 and 3 mm, respectively. An acoustic absorber reduced reflections of the waves at the bottom of the water tank. The tissue phantom (model 040, Computerized Imaging Reference Systems, Inc., Norfolk, VA, USA) mimicked human liver tissue ($\bar{c} = 1539$ m/s and attenuation: 0.5 dB/MHz/cm). The phantom additionally embedded 16 wires, two anechoic regions, and two hyperechoic regions. The axial wire distances from the linear array approximately ranged from 5.8 to 39.7 mm, and the axial and lateral spacings ranged from 1 to 10 mm. The image plane, in both phantoms, crossed the wires to obtain the PSFs.

2) In Vivo: The internal jugular vein and the common carotid artery of a volunteer ($\bar{c} = 1540$ m/s and attenuation: 0.5 dB/MHz/cm) were scanned in the axial plane.

3) Quality Assessment: The single PW images were first assessed by inspecting visually the lateral resolution, the image uniformity, and the intensity of grating lobe artifacts. These artifacts were identified by a two-stage process. First, candidate artifacts were located by searching visually all images for moiré patterns (i.e., patterns of alternating dark and bright areas [28, p. 1]). These patterns result from the interference caused by strong reflectors, such as wires or interfaces, and differ from the usual speckle pattern [29]. The moiré patterns can most easily be detected in hypoechoic regions and decrease in intensity as the number of steering angles increases. Strong reflectors within the estimated bounds (23) of the undesired receive beams near the focal plane are another indicator. Second, the presence of grating lobe artifacts in each candidate area was confirmed by overlaying the image with the receive beams (see Section IV-A) for a focus in the artifact area at multiple frequencies and locating the interference sources. These sources lie in the undesired beams represented by the grating lobes and affect the voxel value (22). The lateral resolution, the reduction of grating lobe artifacts, and the contrast were then measured by the lateral FWHMs of the wires in each phantom, the peak signal-to-noise ratios (PSNRs) of the wires in the wire phantom, and the generalized contrast-to-noise ratios (gCNRs) [30] of the anechoic regions in the tissue phantom, respectively. Each metric produced a spatial distribution (i.e., a set of values that depend on the positions of the wires or the anechoic regions in the FOV). The spatial distributions of the lateral FWHMs and the PSNRs, due to the large numbers of wires, were represented by the medians, the interquartile ranges (IQRs), and the extrema. The medians served as single references for comparisons, whereas the IQRs and the extrema quantified the spatial variability to enable an assessment of the image uniformity. The spatial distributions for the same object and the same number of steering angles, due to the offline processing of the same RF data and, thus, the same realization of the measurement noise, could be compared without statistical tests. These comparisons and those involving different numbers of steering angles, due to the low noise power, likely hold for all noise realizations.

D. Investigated F-Numbers

1) Fixed F-Number: The smallest F-number that eliminated most grating lobe artifacts in the single PW image served as a reference. This F-number, for each object, derived from an F-number sweep that covered the range from 0.1 to 3 with a step size of 0.1.

2) Directivity-Derived F-Numbers: Two F-numbers that seek to ensure a sufficient SNR in the focused RF signal (4) were taken from the literature. Both F-numbers thresholded the element directivity (2) under a specific boundary condition (see Section I) and, thus, were frequency-dependent. This dependence, for the first time, was completely accounted for by the proposed algorithm to assess whether such optimizations of the SNR yield suitable F-numbers. The first F-number, which was proposed by Perrot et al. [6, eqs. (12) and (13)], assumed the array elements to be embedded in a soft baffle [i.e., $o(\alpha) = \cos(\alpha)$] and permitted a maximum attenuation of 3 dB (i.e., $D(\alpha) \geq 0.71$). The result

$$F = \frac{1}{2\tan(\hat{\alpha})} \quad \text{with} \quad \hat{\alpha} = \underset{\alpha\in(0;\pi/2)}{\arg\min} |D(\alpha) - 0.71| \tag{24}$$

required a numerical solution for the acceptance angle $\hat{\alpha}$. This F-number, which will be called "Directivity S3," approximately maintained a constant value of 0.5 for low frequencies and then increased almost linearly up to a value of 2, as shown in Fig. 3. The second F-number, which was proposed by Szabo [19, eq. (10.11)], assumed the array elements to be embedded in a rigid baffle (i.e., $o(\alpha) = 1$) and permitted a maximum attenuation of 6 dB (i.e., $D(\alpha) \geq 0.5$). The half-beamwidth in the focal plane x_6, however, was approximated by $x_6 \approx 0.6\lambda z_\mathrm{f}/w_\mathrm{e}$ and yielded

$$F = \frac{z_\mathrm{f}}{2\ x_6} = \frac{w_\mathrm{e}}{1.2\lambda}. \tag{25}$$

This F-number, which will be called "Directivity R6," increased linearly with the frequency up to a value of 1.5, as shown in Fig. 3.

V. Results

A. Receive Beam in the Focal Plane

The beam profiles revealed the grating lobe positions and a tradeoff between the lateral main lobe width and the GLL, as shown in Fig. 5. The first-order grating lobes entered the FOV for normalized element pitches $\bar{p}_\mathrm{e}$ exceeding 0.7. The estimated bounds of these lobes (23) agreed with the actual bounds for angular distances $\chi_\mathrm{ub}, -\chi_\mathrm{lb} > 30°$. Note that negative angles (see Fig. 2) resulted in positive lateral distances. The beams were identical if the given F-numbers fell below the minimum F-number that could be achieved by the linear array for the selected focus (i.e., $F_\mathrm{l} \approx 0.55$). The full aperture consistently yielded the smallest FWHMs but the largest GLLs for all frequencies. The dynamic aperture with a fixed F-number, conversely, yielded the largest FWHMs but the smallest GLLs. All frequency-dependent F-numbers ranged between these two extremes. The proposed F-number (21), however, effectively reduced the lateral FWHMs of the main lobe to the same value as the full aperture (i.e., FWHM $\leq$ 1.1 mm) and additionally limited the GLLs to the same value as the fixed F-number (i.e., GLL ≤ -27 dB).

B. Parameter Sweeps

The proposed F-number (21) limited the GLL, as shown in Fig. 6. The GLLs in Fig. 6(a) strongly resemble the angular distances of the first-order grating lobes (see Fig. 3). This notion is confirmed by the presentation of the GLLs as a function of the minimum angular distance χ_0, as shown in Fig. 6(b). The GLL, for a fixed minimum angular distance χ_0 and low frequencies, increased initially due to the lobe

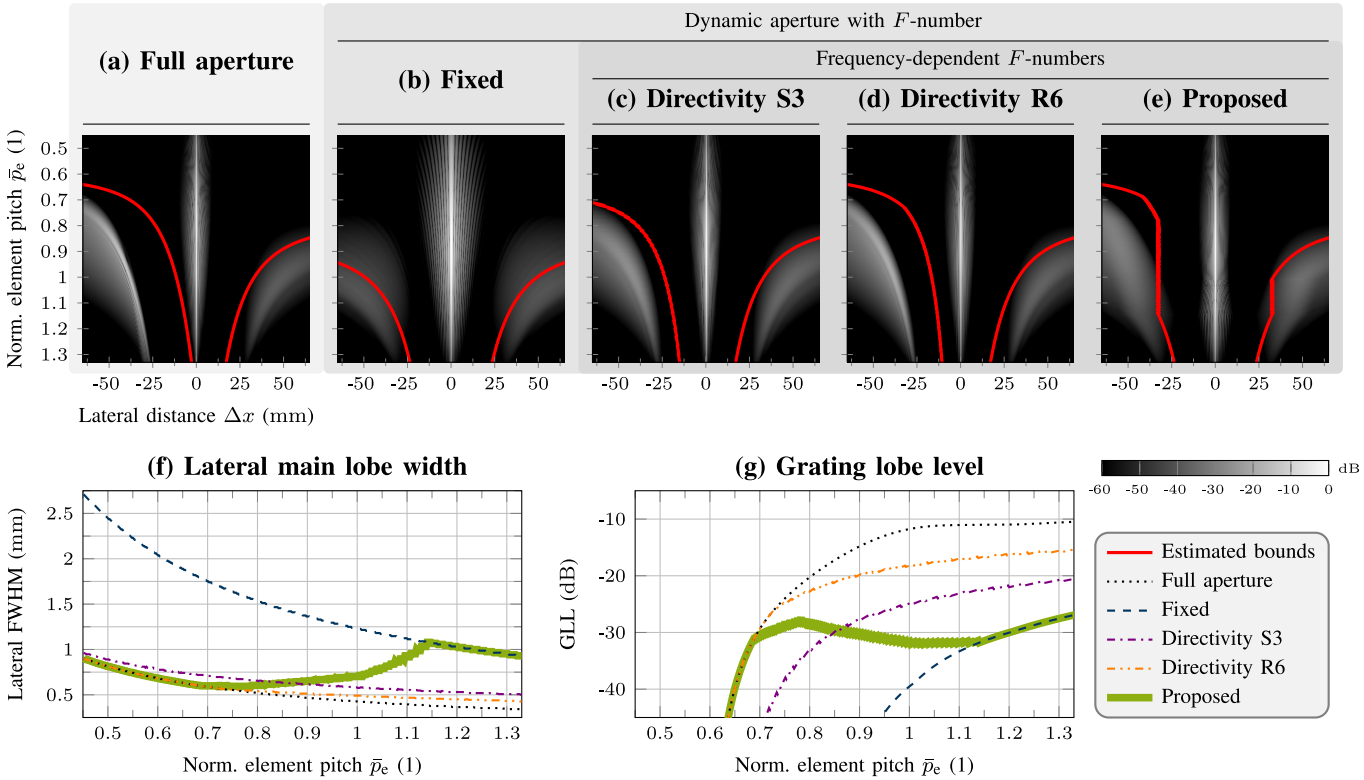

Fig. 5. Effect of all apertures on the receive beam in the focal plane. Only the dynamic aperture with the proposed *F*-number (21) reduced the lateral width of the main lobe and additionally limited the maximum amplitude of the grating lobes. The images show the absolute values of the receive beam (29) as functions of the normalized element pitch $\bar{p}_e = p_e/\lambda$ and the lateral distance $\Delta x = x_0 - x_f$ for (a) full aperture and (b)–(e) dynamic apertures with various *F*-numbers. These *F*-numbers include (b) fixed *F*-number of $F = 3$, (c) directivity-derived *F*-number (24), (d) directivity-derived *F*-number (25), and (e) proposed *F*-number (21) with $\chi_0 = 45°$, $F_{ub} = 3$, and $\delta = 10°$. The lateral main lobe width is measured by (f) lateral FWHM, and the maximum grating lobe amplitude is assessed by (g) GLL.

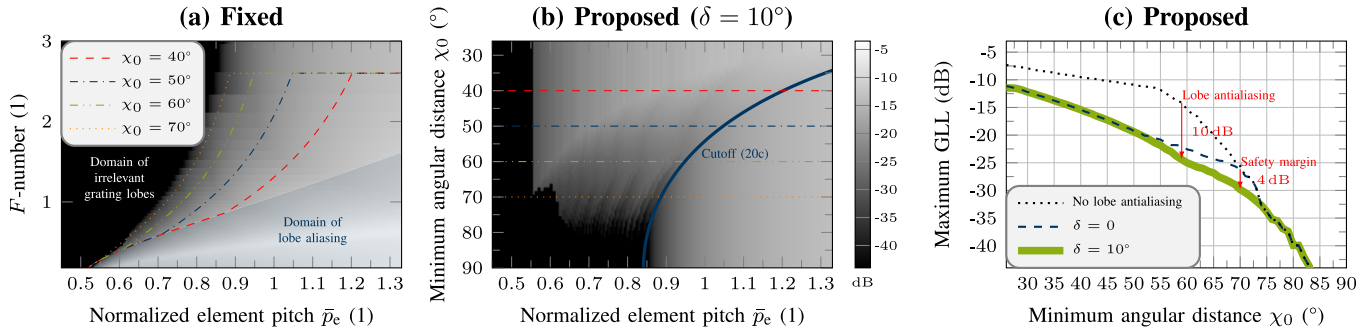

Fig. 6. Effect of the *F*-number and the frequency on the GLL of the receive beam in the focal plane. The minimum angular distance χ_0, which the proposed *F*-number (21) imposed on the first-order grating lobes, controlled the maximum GLL, and the lobe antialiasing bound (19) prevented large GLLs of up to -3.5 dB. The images show the GLLs as functions of the normalized element pitch $\bar{p}_e = p_e/\lambda$ and (a) given *F*-number or (b) minimum angular distance χ_0 in the proposed *F*-number (21) with $F_{ub} = 2.6$ and $\delta = 10°$. Curves show (c) maximum GLL for a normalized element pitch $\bar{p}_e$ in the interval $[0.45; \bar{p}_{e,ub}]$, where $\bar{p}_{e,ub}$ is the cutoff (20c), as a function of the minimum angular distance χ_0.

antialiasing bound (19). The GLL peaked at the transition frequency, where the minimum angular distance bound (20) exceeded the lobe antialiasing bound (19) and then stayed roughly constant, similar to the example in Fig. 5(g). The GLL increased once the maximum permissible *F*-number F_{ub} was achieved at the cutoff frequency (20c). The lobe antialiasing, as shown in Fig. 6(c), reduced the maximum GLL by up to 10 dB. The increase of the safety margin from $\delta = 0°$ to $\delta = 10°$ reduced this metric by up to 4 dB. Larger safety margins (i.e., $\delta > 10°$) did not further reduce this metric.

C. B-Mode Image Formation

The receive aperture strongly affected the B-mode images, as shown in Fig. 7. The full aperture maximized the lateral resolution at the expense of both image uniformity and grating lobe artifacts, as shown in Fig. 7(a). The image quality varied significantly across the FOV because the actual *F*-numbers (10) increased with the axial position and diverged with the lateral position. The grating lobe artifacts near the edges of the linear array rendered the images unusable in clinical practice. The dynamic aperture with a fixed *F*-number, in contrast, increased the image uniformity and eliminated most grating

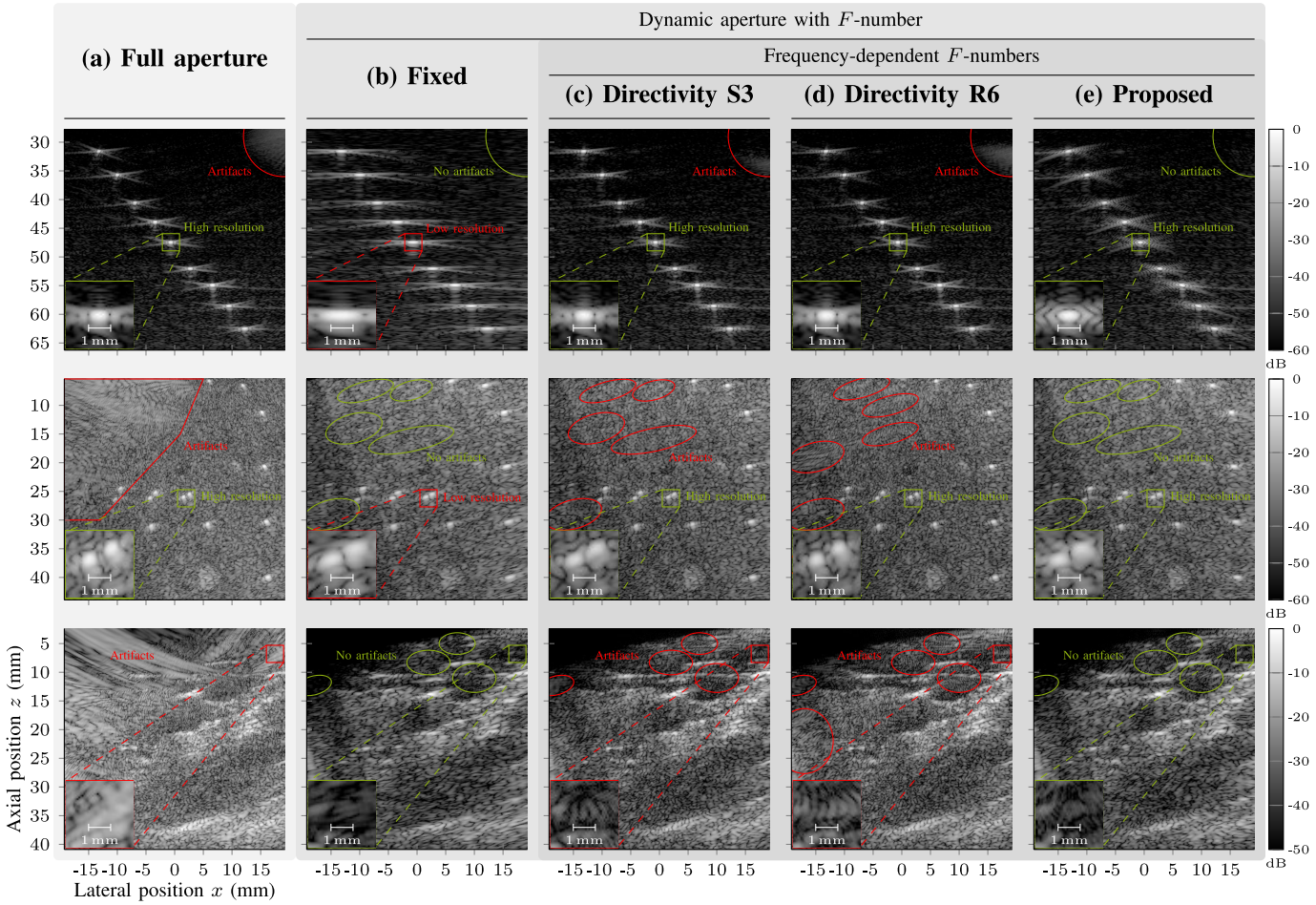

Fig. 7. Single PW images of the wire phantom (top row), the tissue phantom (center row), and the common carotid artery (in vivo, bottom row). Only the proposed F-number (21) eliminated most grating lobe artifacts and reduced the associated loss in the lateral resolution. Grating lobe artifacts resemble moiré patterns (i.e., patterns of alternating dark and bright areas). These patterns differ from the usual speckle pattern and can most easily be detected in hypoechoic regions. The images show the absolute voxel values (22) for (a) full aperture and (b)–(e) dynamic apertures with various F-numbers. These F-numbers include (b) fixed F-numbers of $F = \{3, 1.5, 2\}$ (top to bottom row), (c) directivity-derived F-number (24), (d) directivity-derived F-number (25), and (e) proposed F-number (21) with $\chi_0 = \{40°, 60°, 80°\}$, $F_{\text{ub}} = \{3, 1.5, 2\}$, and $\delta = 10°$. The inset images magnify the regions indicated by the squares. These regions either contain wires (top and center rows) or grating lobe artifacts (bottom row). The ellipses indicate additional locations of grating lobe artifacts. The red color denotes a low resolution or the presence of artifacts. The green color denotes a high resolution or the reduction of artifacts.

lobe artifacts at the expense of the lateral resolution, as shown in Fig. 7(b). The image uniformity resulted from the control of the actual F-numbers (10). This control most affected small axial positions and only failed near the lateral bounds of the FOV, where the asymmetry of the aperture reduced the lateral resolution. The reduction of the grating lobe artifacts agreed with the minimum GLLs for all frequencies [see Fig. 5(g)]. The loss in the lateral resolution, likewise, agreed with the maximum FWHMs of the main lobe for all frequencies [see Fig. 5(f)]. All frequency-dependent F-numbers reduced this resolution loss, as shown in Fig. 7(c)–(e). Both directivity-derived F-numbers (24) and (25), however, reintroduced grating lobe artifacts (see ellipses). These artifacts were less severe for the F-number (24), which used the soft baffle boundary condition. Only the proposed F-number (21) reduced grating lobe artifacts to a similar extent as the fixed F-number. The fluctuations of the lateral FWHMs of the main lobe with the frequency [see Fig. 5(f)] caused oscillating sidelobes in the PSFs, as shown in the top row of Fig. 7(e).

The image quality metrics confirmed the above findings and demonstrated the effect of the coherent compounding, as shown in Fig. 8. The full aperture and the dynamic aperture with a fixed F-number consistently achieved the minimum and maximum median lateral FWHMs, respectively, as shown in Fig. 8(a) and (b). All frequency-dependent F-numbers ranged between these two extremes. The proposed F-number (21) increased the median lateral FWHMs in comparison to both directivity-derived F-numbers (24) and (25) but reduced this metric in comparison to the fixed F-number by up to 0.61 mm (46.8%) for the wire phantom and 0.12 mm (14.9%) for the tissue phantom. The proposed F-number (21), however, also eliminated grating lobe artifacts and achieved the best median PSNRs, as shown in Fig. 8(c). The median PSNRs increased by up to 9.9 dB (21.2%) in comparison to the full aperture. The contrast of the shallow anechoic region (diameter: 2 mm) increased with smaller lateral FWHMs of the wires, as shown in Fig. 8(d). The frequency-dependent F-numbers thus improved this contrast by up to 13.1% in comparison

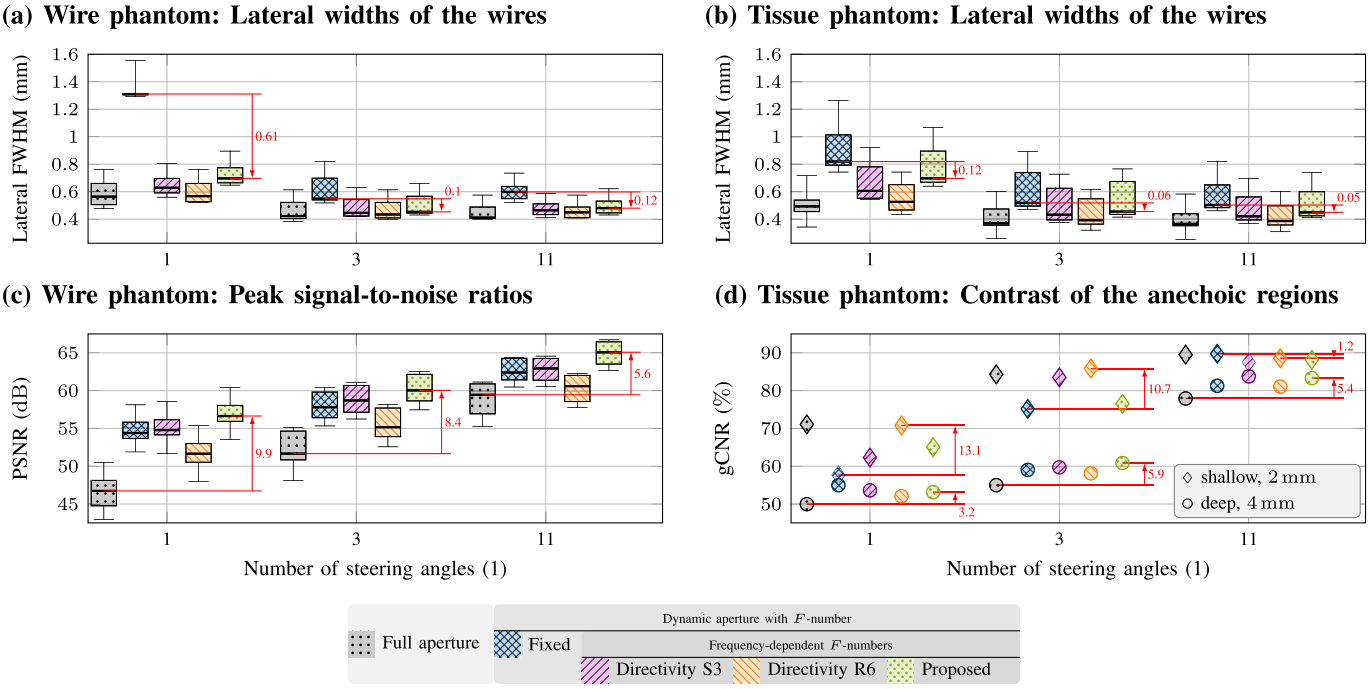

Fig. 8. Effect of all receive apertures on the B-mode image quality. All dynamic apertures with frequency-dependent *F*-numbers, in comparison to the fixed *F*-number, significantly reduced the lateral FWHMs of the wires in both phantoms. Only the proposed *F*-number (21), however, also eliminated grating lobe artifacts and, thus, achieved the best PSNRs. Each distribution describes the spatial variability of a metric in a single B-mode image (i.e., the statistical sample size is unity). The horizontal lines indicate the medians, the boxes show the IQRs, and the whiskers represent the extrema. Overlaps between adjacent distributions can result from similar values of the metrics at different locations in the FOV. The metrics include (a) lateral FWHMs of the wires in the wire phantom, (b) lateral FWHMs of the wires in the tissue phantom, (c) PSNRs of the wires in the wire phantom, and (d) gCNRs of the anechoic regions in the tissue phantom.

to the fixed F-number. The contrast of the deep anechoic region (diameter: 4 mm), however, increased with the PSNRs of the wires. The proposed F-number (21) thus improved this contrast by up to 5.9% in comparison to the full aperture. The coherent compounding improved all quality metrics and reduced the differences between the receive apertures.

VI. Discussion

Dynamic receive apertures, according to the differences in the B-mode image quality (see Figs. 7 and 8), are essential for ultrafast UI with linear arrays. The frequency-dependent F-numbers, in comparison to the fixed F-number (1), improve the lateral resolution by widening the aperture for low frequencies. The complex-valued apodization weights (7) implement a low-pass filter [see Fig. 4(b)], whose cutoff frequency decreases with increasing lateral distance between the array element and the focus. The grating lobe artifacts, as expected, dispute the derivation of F-numbers from the element directivity (2). Both directivity-derived F-numbers (24) and (25) ignore grating lobes, which are more important than the measurement noise (see Section I), and, thus, reduced image artifacts less effectively than the proposed F-number (21). This F-number reduced grating lobe artifacts by two mechanisms. First, it steered the grating lobes away from the wires in the top-left corner of the wire phantom using a minimum angular distance of $\chi_0 = 40°$ [see the top row in Fig. 7(e)]. Second, it limited the GLL [see Fig. 6(c)] in both remaining objects, where the grating lobes always caused interference.

The derivation of the proposed F-number (21) relied on the far-field directivity pattern (14) because, to the best knowledge of the authors, a simple and accurate analytic expression for the grating lobes in the focal plane does not exist. The method of stationary phase (see Appendix B-B), unfortunately, fails for the receive beam, which is represented by the inverse transverse Fourier transform (29a), because the far-field directivity pattern (14), as shown in Fig. 2, oscillates too quickly as a function of the angle [31]. A selection of the F-number based on numerical results, such as the GLL shown in Fig. 6(a), however, could be more accurate. Wilcox and Zhang [13, Fig. 5 and eq. (32)], for example, derived an empirical expression for a fixed F-number (1) from simulated PSFs in SA imaging. This expression, surprisingly, equals the lobe antialiasing bound (19) with a safety margin of $\delta = 0$ at the center frequency.

The computational costs of the proposed algorithm exceed those of the DAS algorithm. The proposed algorithm executes the DAS algorithm for each frequency and requires additional FFTs of the RF signals. The apodization weights (7), however, are independent of the RF signals and can be precomputed. The Fourier domain, moreover, permits the independent processing of different frequencies and, thus, lends itself to multithreading on massively parallel architectures. The running times of an exemplary CUDA implementation ranged from 20 to 40 s on a GeForce GTX 1080 Ti (NVIDIA Corporation, Santa Clara, CA, USA). The authors speculate that a simplified algorithm based on filter banks [32, Fig. 4.] and the usage of a fixed F-number in each band can achieve

similar benefits at reduced costs. Such a simplification, however, requires the proposed algorithm as a benchmark. The authors maintain a public version of the source code [33] to support the reproduction of the results and facilitate further research.

The acoustic reciprocity ensures that the proposed F-number (21) also holds for the transmit focusing. Element-specific excitation voltages, which result from the complex-valued apodization weights (7), thus control the grating lobes in the syntheses of focused beams or diverging waves with virtual sources. A suppression of both transmit and receive grating lobes may further improve the image quality.

Only a few nonadaptive methods suppress grating lobes in ultrafast UI. Bae and Song [34] optimized the steering angles of the transmitted PWs to suppress transmit grating lobes in CPWC. The method, however, requires tens of steering angles and, thus, limits the frame rate. Ponnle et al. [16] modulated the focused receive beams in sector scans depending on the steering angle. This method, unlike the proposed method, uses beam steering. Heller and Schmitz [35] exploited the lateral motion of the array to decrease the element pitch of a synthetic receive aperture. The motion-induced shift, however, must be known exactly. Kou et al. [36] superimposed the envelope images created by three different apodization schemes in the receive focusing. The envelope detection, however, is nonlinear and removes phase information. Wojcik et al. [29] averaged the RF signals provided by adjacent elements to synthesize a receive aperture with half the element pitch. The method, however, only suppresses odd-order grating lobes and relies on boxcar windows.

VII. Conclusion

Dynamic receive apertures with a fixed F-number (1) are a standard in ultrafast UI with linear arrays. This article has proposed a frequency-dependent F-number (21) that reduces grating lobe artifacts to a similar extent as a fixed F-number (1) but additionally improves the lateral resolution. Experiments with a Fourier-domain beamforming algorithm showed improvements in the lateral resolution by up to 46.8% in comparison to fixed F-numbers (1). Grating lobe artifacts are reduced by up to 9.9 dB in comparison to the full aperture. The proposed F-number (21) thus outperformed two F-numbers that were recently derived from the element directivity (2) in the reduction of image artifacts. The presented theory improves the understanding of dynamic apertures and facilitates the F-number selection.

Appendix A

The far-field directivity pattern of the focused aperture will now be derived and the underlying simplifications will be justified. To simplify the notation, the dependence of all variables on the focus $\mathbf{r}_\mathrm{f}$ and the frequency f will usually be omitted. The scattering of the transmitted acoustic pressure field $p^{(\mathrm{tx})}(\mathbf{r})$ by the image voxel at the position $\mathbf{r}_0 = (x_0, 0, z_0)^\mathrm{T}$ results in the acoustic pressure field [14, eq. (5.33)], [21, eq. (6.53)]

$$p^{(\mathrm{sc})}(\mathbf{r}) = P(\mathbf{r}_0)\, g(\mathbf{r} - \mathbf{r}_0) \tag{26a}$$

at the position $\mathbf{r} = (x, y, z)^\mathrm{T}$, where $P(\mathbf{r}_0) = \underline{k}^2 \Delta V \epsilon(\mathbf{r}_0) p^{(\mathrm{tx})}(\mathbf{r}_0)$ is the amplitude, $\underline{k} = \beta - j\alpha$ is the complex-valued wavenumber with the phase term $\beta = 2\pi/\lambda$ and the absorption coefficient α, ΔV is the voxel volume, $\epsilon(\mathbf{r}_0)$ is the echogenicity, and g is Green's function

$$g(\mathbf{r}) = -\frac{1}{4\pi} \frac{e^{-j\underline{k}\|\mathbf{r}\|_2}}{\|\mathbf{r}\|_2} \tag{26b}$$

with the ℓ_2-norm $\|\mathbf{r}\|_2 = (x^2 + y^2 + z^2)^{1/2}$.

The Fourier coefficients of the acquired RF signals (5) result from the transduction of the force exerted by the acoustic pressure field (26) on the face L_m of the mth array element [14, p. 299], [37, eq. (9.13)]. These coefficients, neglecting the elevational focusing by the acoustic lens [8], equal

$$U_m = 2\, h^{(\mathrm{rx})} \int_{\mathrm{L}_m} p^{(\mathrm{sc})}(\mathbf{r}_\rho, 0) \mathrm{d}\mathbf{r}_\rho$$

where the factor of 2 accounts for a rigid baffle, $h^{(\mathrm{rx})}$ is the common electromechanical transfer function of all receive channels, and $\mathbf{r}_\rho = (x, y)^\mathrm{T}$ is the transverse position. The Fourier coefficients of the focused RF signal (6) thus read

$$U^{(\mathrm{foc})}(\mathbf{r}_\mathrm{f}) = C(\mathbf{r}_0) \int_{\mathbb{R}^2} s(\mathbf{r}_\rho) g(x - x_0, y, -z_0) \mathrm{d}\mathbf{r}_\rho \tag{27}$$

where $C(\mathbf{r}_0) = 2\, h^{(\mathrm{rx})} P(\mathbf{r}_0)$ denotes the amplitude and $s(\mathbf{r}_\rho)$ is the aperture function. This function equals

$$s(\mathbf{r}_\rho) = \mathrm{rect}\left(\frac{y}{h_\mathrm{e}}\right) \sum_{m=0}^{N_\mathrm{e}-1} w_m(\mathbf{r}_\mathrm{f}, f)\, \mathrm{rect}\left(\frac{x - x_{\mathrm{e},m}}{w_\mathrm{e}}\right) \tag{28a}$$

and uses the products of the rectangle function

$$\mathrm{rect}(x) = \begin{cases} 1, & \text{for } |x| < 1/2 \\ 0, & \text{for } |x| > 1/2 \end{cases} \tag{28b}$$

to represent all faces L_m of the array elements.

The Fourier coefficients (27) can be related to the far-field directivity pattern of the focused aperture by a PW expansion of Green's function (26b). This so-called Weyl expansion reads [21, eq. (4.4)]

$$g(\mathbf{r}) = \frac{j\gamma}{8\pi^2} \int_{\mathbb{R}^2} \frac{e^{-j\gamma[\langle \bar{\mathbf{k}}_\rho, \mathbf{r}_\rho \rangle + \bar{k}_z(\bar{\mathbf{k}}_\rho)|z|]}}{\bar{k}_z(\bar{\mathbf{k}}_\rho)} \mathrm{d}\bar{\mathbf{k}}_\rho$$

where $\gamma = \beta(1 - (\alpha/\beta)^2)^{1/2}$ is a reference phase term, $\bar{\mathbf{k}}_\rho = (\bar{k}_x, \bar{k}_y)^\mathrm{T}$ are the normalized transverse frequencies, $\langle \bar{\mathbf{k}}_\rho, \mathbf{r}_\rho \rangle = \bar{k}_x x + \bar{k}_y y$ is the dot product, and $\bar{k}_z(\bar{\mathbf{k}}_\rho)$ is the complex-valued square root

$$\bar{k}_z(\bar{\mathbf{k}}_\rho) = \sqrt{1 - \|\bar{\mathbf{k}}_\rho\|_2^2 - j\frac{2\alpha\beta}{\gamma^2}}$$

with $\mathrm{Im}\{\bar{k}_z(\bar{\mathbf{k}}_\rho)\} \leq 0$. The insertion of this expansion into (27) yields the inverse transverse Fourier transform

$$U^{(\mathrm{foc})}(\mathbf{r}_\mathrm{f}) = \frac{j\gamma C(\mathbf{r}_0)}{8\pi^2} \times \int_{\mathbb{R}^2} \frac{S(\bar{\mathbf{k}}_\rho) e^{-j\gamma \bar{k}_z(\bar{\mathbf{k}}_\rho) z_0}}{\bar{k}_z(\bar{\mathbf{k}}_\rho)} e^{j\gamma \bar{k}_x x_0} \mathrm{d}\bar{\mathbf{k}}_\rho \tag{29a}$$

where $S(\bar{\mathbf{k}}_\rho)$ denotes the far-field directivity pattern

$$S(\bar{\mathbf{k}}_\rho) = \int_{\mathbb{R}^2} s(\mathbf{r}_\rho) e^{-j\gamma\langle \bar{\mathbf{k}}_\rho, \mathbf{r}_\rho\rangle} \mathrm{d}\mathbf{r}_\rho. \tag{29b}$$

This result has a simple interpretation. The far-field directivity pattern (29b) describes the sensitivity of the focused aperture to incoming PWs with the wave vectors

$$\mathbf{k}(\bar{\mathbf{k}}_\rho) = \gamma\left[\bar{\mathbf{k}}_\rho, -\bar{k}_\mathrm{z}(\bar{\mathbf{k}}_\rho)\right]^\mathrm{T}. \tag{30}$$

These PWs, for small normalized transverse frequencies (i.e., $\|\bar{\mathbf{k}}_\rho\|_2 < 1$), are propagable and contribute to the focused RF signal. Propagable PWs are either homogeneous (if $\alpha = 0$) or weakly inhomogeneous (if $\alpha > 0$). The PWs, for large normalized transverse frequencies (i.e., $\|\bar{\mathbf{k}}_\rho\|_2 > 1$), however, are evanescent and may be neglected due to a strong attenuation along the z-axis. Hence, the far-field directivity pattern (29b) for $\|\bar{\mathbf{k}}_\rho\|_2 < 1$ suffices.

Soft tissues permit two simplifications. First, the phase velocities $c(f)$ in different tissues are similar and almost independent of the frequency [38]. This justifies the simplification $\bar{c} \approx c(f) = \lambda f \approx 1500$ m/s, where $\bar{c}$ denotes the average speed of sound in the arrival times (12). Second, both the absorption coefficient α and the phase term β increase almost linearly with the frequency [38]. The slopes, which typically amount to 1 dB/MHz/cm for the absorption coefficient and $2\pi/c(f) \approx 42$/MHz/cm for the phase term, however, significantly differ. This difference justifies the assumption $\alpha/\beta \approx 0.27\% \ll 1$ and the simplification $\gamma \approx \beta$. The far-field directivity pattern (29b), inserting the aperture function (28), thus reduces to

$$S(\bar{\mathbf{k}}_\rho) = \hat{S}(\mathbf{r}_\mathrm{f}) \operatorname{sinc}\left(\bar{k}_x \frac{w_\mathrm{e}}{\lambda}\right) \operatorname{sinc}\left(\bar{k}_\mathrm{y} \frac{h_\mathrm{e}}{\lambda}\right) \hat{H}(\bar{k}_x) \tag{31a}$$

with $\hat{S}(\mathbf{r}_\mathrm{f}) = w_\mathrm{e} h_\mathrm{e} e^{j\beta d^{(\mathrm{tx})}(\mathbf{r}_\mathrm{f})}$ and the discrete-space Fourier transform (DSFT)

$$\hat{H}(\bar{k}_x) = \sum_{m=0}^{N_\mathrm{e}-1} \bar{a}_m(\mathbf{r}_\mathrm{f}, f) e^{-j\beta\left[\bar{k}_x x_{\mathrm{e},m} - d_m^{(\mathrm{tx})}(\mathbf{r}_\mathrm{f})\right]}. \tag{31b}$$

The array geometry permits a final simplification. The element height h_e usually equals multiple wavelengths λ (i.e., $h_\mathrm{e} \gg \lambda$) [14, p. 447]. The sinc functions, thus, rapidly decrease the pattern (31) in modulus with increasing normalized elevational frequency $\bar{k}_\mathrm{y}$. They limit the reception to PWs that propagate parallel to the image plane. This property justifies the simplification $\bar{k}_\mathrm{y} \approx 0$ and the treatment of the pattern (31) as a univariate function of the normalized lateral frequency $\bar{k}_x$ [see (14)]. This frequency, after the real part of the wave vector (30), defines the angle $\alpha = \arcsin(\bar{k}_x)$ at which the PW with the direction $\mathbf{e}_\alpha = (\sin(\alpha), 0, -\cos(\alpha))^\mathrm{T}$ arrives at the aperture if $|\bar{k}_x| < 1$.

APPENDIX B

The DSFT (31b) in the far-field directivity pattern (31) lacks a simple form and must be approximated to derive the bounds of the main (16) and grating lobes (17). The proposed approximation consists of two steps. First, the Poisson summation formula [24, Th. 6.4], [25, Th. 2.4] is used to show that the evaluation of a single Fourier transform $H(\bar{k}_x)$ suffices to determine the DSFT (31b). The DSFT (31b), in fact, superimposes weighted and shifted copies of the Fourier transform $H(\bar{k}_x)$. Each copy, upon multiplication by the sinc functions in (31a), creates a lobe (14b) in the far-field directivity pattern (14). The Fourier transform $H(\bar{k}_x)$ creates the main lobe, and the copies create the grating lobes. The Fourier transform $H(\bar{k}_x)$, however, lacks a closed form and, thus, prevents analysis. Second, the method of stationary phase [39, Ch. 4] is used to approximate the Fourier transform $H(\bar{k}_x)$ in closed form and, by superimposing weighted and shifted copies of the result, the DSFT (31b). This approximation predicts low-pass band limits (i.e., there are lower and upper bounds $\bar{k}_{x,\mathrm{lb}} \in (-1; 0)$ and $\bar{k}_{x,\mathrm{ub}} \in (0; 1)$, respectively, such that $|H(\bar{k}_x)| \approx 0$ for $\bar{k}_x < \bar{k}_{x,\mathrm{lb}}$ or $\bar{k}_x > \bar{k}_{x,\mathrm{ub}}$). These band limits not only equal the main lobe bounds (16) but can also be used to predict the grating lobes bounds (15) and (17).

A. Poisson Summation Formula

The first step requires a continuous function $h(x)$ whose samples $h(x_{\mathrm{e},m})$ at the lateral center coordinates (3) explain the DSFT (31b). This function describes a continuous focused aperture and reads

$$h(x) = \bar{a}(x, \mathbf{r}_\mathrm{f}, f) e^{j\beta\sqrt{(x-x_\mathrm{f})^2 + z_\mathrm{f}^2}} \tag{32}$$

where $\beta = 2\pi/\lambda$ is the wavenumber and $\bar{a}(x, \mathbf{r}_\mathrm{f}, f)$ is a continuous version of the apodization weights (11). This version simply evaluates the window function (11a) in the numerator of (11b) at arbitrary lateral positions x. The version, hence, vanishes outside the aperture [i.e., $\bar{a}(x, \mathbf{r}_\mathrm{f}, f) = 0$ for all $x \le x_\mathrm{l}$ or $x \ge x_\mathrm{r}$ with the lateral bounds (9)] and equals the weights (11) within [i.e., $\bar{a}(x_{\mathrm{e},m}, \mathbf{r}_\mathrm{f}, f) = \bar{a}_m(\mathbf{r}_\mathrm{f}, f)$ for all $m \in \mathbb{A}(\mathbf{r}_\mathrm{f}, f)$ with the set (8)]. The DSFT (31b), according to the Poisson summation formula, then equals

$$\hat{H}(\bar{k}_x) = \sum_{l=-\infty}^{\infty} \tau_l H(\bar{k}_x - l\bar{k}_\mathrm{s}) \tag{33a}$$

where $\tau_l = (-1)^{l(N_\mathrm{e}-1)}/p_\mathrm{e}$ are weights, $\bar{k}_\mathrm{s} = \lambda/p_\mathrm{e}$ is the normalized lateral sampling frequency, and

$$H(\bar{k}_x) = \int_{-\infty}^{\infty} h(x) e^{-j\beta\bar{k}_x x} \mathrm{d}x \tag{33b}$$

is the Fourier transform of the function (32). The superposition (33a) consists of weighted copies of the Fourier transform (33b), each shifted by an integer multiple of the normalized lateral sampling frequency $\bar{k}_\mathrm{s}$. Each summand, upon multiplication by the sinc functions in (31a), creates a lobe (14b) in the far-field directivity pattern (14). The summand for $l = 0$ creates the main lobe. The remaining summands create infinitely many grating lobes, and the integer $l \neq 0$ denotes their order.

B. Approximation by the Method of Stationary Phase

The Fourier transform (33b) lacks a closed form and, thus, prevents analysis. The properties of the integrand, however,

enable the method of stationary phase [39, Ch. 4] to approximate this transform in closed form. The integral, substituting the normalized lateral position $\bar{x} = (x - x_\mathrm{f})/z_\mathrm{f}$, becomes

$$H(\bar{k}_x) = z_\mathrm{f} e^{-j\beta \bar{k}_x x_\mathrm{f}} \times \int_{\bar{x}_\mathrm{l}}^{\bar{x}_\mathrm{r}} \bar{a}(x_\mathrm{f} + \bar{x} z_\mathrm{f}, \mathbf{r}_\mathrm{f}, f) e^{-j\sigma\phi(\bar{x})} \mathrm{d}\bar{x} \tag{34a}$$

where the endpoints of the integration interval $\bar{x}_\mathrm{l} = (x_\mathrm{l} - x_\mathrm{f})/z_\mathrm{f} = -1/(2F_\mathrm{l})$ and $\bar{x}_\mathrm{r} = (x_\mathrm{r} - x_\mathrm{f})/z_\mathrm{f} = 1/(2F_\mathrm{r})$ derive from the actual F-numbers (10), the parameter $\sigma = \beta z_\mathrm{f} = 2\pi \bar{z}_\mathrm{f}$ with the focal length-to-wavelength ratio $\bar{z}_\mathrm{f} = z_\mathrm{f}/\lambda$ indicates the oscillation frequency, and the phase $\phi(\bar{x})$ reads

$$\phi(\bar{x}) = \bar{k}_x \bar{x} - \sqrt{1 + \bar{x}^2}. \tag{34b}$$

The focal length z_f usually exceeds multiple wavelengths (i.e., $\bar{z}_\mathrm{f} \gg 1$). The parameter σ, hence, exceeds 2π (i.e., $\sigma \gg 2\pi$), and the complex exponential function oscillates quickly across the receive aperture. The apodization weights, in contrast, slowly modulate the amplitude of the oscillations. In the limit $\sigma \to \infty$, only critical positions of the phase (34b) contribute to the integral. Such positions include stationary positions, where the first derivative vanishes, and integration endpoints.

The first and second derivatives of the phase (34b) with respect to the normalized lateral position $\bar{x}$ equal

$$\phi'(\bar{x}) = \bar{k}_x - \frac{\bar{x}}{\sqrt{1 + \bar{x}^2}} \quad \text{and} \quad \phi''(\bar{x}) = -\frac{1}{\sqrt{1 + \bar{x}^2}^3}$$

respectively, and show that a local maximum exists at the stationary position

$$\bar{x}_\mathrm{s} = \frac{\bar{k}_x}{\sqrt{1 - \bar{k}_x^2}}. \tag{35}$$

This position, as the normalized lateral frequency $|\bar{k}_x| < 1$ increases, moves from negative infinity across the aperture to positive infinity. The position coincides with the integration endpoints $\bar{x}_\mathrm{l}$ and $\bar{x}_\mathrm{r}$ for $\bar{k}_x = \bar{k}_{x,\mathrm{lb}} = -1/(1 + (2F_\mathrm{l})^2)^{1/2}$ and $\bar{k}_x = \bar{k}_{x,\mathrm{ub}} = 1/(1 + (2F_\mathrm{r})^2)^{1/2}$, respectively. This coincidence requires a special version of the stationary phase method that unifies the treatment of the stationary position (35) and the integration endpoints [39, Secs. 4.1a and 4.6a].

The Fourier transform (34), inserting the second-order Taylor polynomial of the phase (34b) about the stationary position

$$\phi(\bar{x}) \approx \phi(\bar{x}_\mathrm{s}) + \frac{\phi''(\bar{x}_\mathrm{s})}{2} (\bar{x} - \bar{x}_\mathrm{s})^2$$

with the coefficients

$$\phi(\bar{x}_\mathrm{s}) = -\sqrt{1 - \bar{k}_x^2} \quad \text{and} \quad \phi''(\bar{x}_\mathrm{s}) = -\sqrt{1 - \bar{k}_x^2}^3$$

adding $0 = \bar{a}(x_\mathrm{f} + \bar{x}_\mathrm{s} z_\mathrm{f}, \mathbf{r}_\mathrm{f}, f) - \bar{a}(x_\mathrm{f} + \bar{x}_\mathrm{s} z_\mathrm{f}, \mathbf{r}_\mathrm{f}, f)$ to the apodization weights, and integrating by parts, meets

$$H(\bar{k}_x) \approx z_\mathrm{f} e^{-j\beta \bar{k}_x x_\mathrm{f}} e^{-j\sigma\phi(\bar{x}_\mathrm{s})} \big[H_1(\bar{k}_x) + H_2(\bar{k}_x) \big] \tag{36a}$$

where the summands read

$$H_1(\bar{k}_x) = \bar{a}(x_\mathrm{f} + \bar{x}_\mathrm{s} z_\mathrm{f}, \mathbf{r}_\mathrm{f}, f) \sqrt{\frac{\pi}{2\sigma |\phi''(\bar{x}_\mathrm{s})|}} \times e^{-j3\pi/4} \operatorname{erf}\left[(\bar{x} - \bar{x}_\mathrm{s}) \sqrt{\frac{\sigma |\phi''(\bar{x}_\mathrm{s})|}{2}} e^{j3\pi/4} \right] \Bigg|_{\bar{x}_\mathrm{l}}^{\bar{x}_\mathrm{r}} \tag{36b}$$

with the error function [40, eq. (7.2.1)]

$$\operatorname{erf}(x) = \frac{2}{\sqrt{\pi}} \int_0^x e^{-\tau^2} \mathrm{d}\tau$$

and

$$H_2(\bar{k}_x) = \frac{j e^{-j\sigma\phi''(\bar{x}_\mathrm{s})(\bar{x} - \bar{x}_\mathrm{s})^2/2}}{\sigma \phi''(\bar{x}_\mathrm{s})} \times \frac{\bar{a}(x_\mathrm{f} + \bar{x} z_\mathrm{f}, \mathbf{r}_\mathrm{f}, f) - \bar{a}(x_\mathrm{f} + \bar{x}_\mathrm{s} z_\mathrm{f}, \mathbf{r}_\mathrm{f}, f)}{\bar{x} - \bar{x}_\mathrm{s}} \Bigg|_{\bar{x}_\mathrm{l}}^{\bar{x}_\mathrm{r}}. \tag{36c}$$

The first summand $H_1(\bar{k}_x)$, which is of the order $1/\sqrt{\sigma}$ and, thus, most important, describes the contribution of the aperture. The second summand $H_2(\bar{k}_x)$, which is of the order $1/\sigma$ and, thus, less important, provides corrections required by the edges of the aperture. This summand, as the stationary position (35) approaches the integration endpoints, depends on the derivatives of the apodization weights $\bar{a}(x, \mathbf{r}_\mathrm{f}, f)$. Both summands show that the Fourier transform (34) approximates zero if the stationary position (35) leaves the receive aperture [i.e., $|H(\bar{k}_x)| \approx 0$ for $\bar{k}_x < \bar{k}_{x,\mathrm{lb}}$ or $\bar{k}_x > \bar{k}_{x,\mathrm{ub}}$; see (16)]. The approximation error, which is of the order $1/\sigma^2$, decreases with the square of the focal length-to-wavelength ratio $\bar{z}_\mathrm{f}$ and, thus, is usually small. The grating lobes, according to the superposition (33a), extend from $l\bar{k}_\mathrm{s} + \bar{k}_{x,\mathrm{lb}}$ to $l\bar{k}_\mathrm{s} + \bar{k}_{x,\mathrm{ub}}$ with $l \neq 0$ [see (15) and (17)].

References

[1] J. Jensen, M. B. Stuart, and J. A. Jensen, "Optimized plane wave imaging for fast and high-quality ultrasound imaging," *IEEE Trans. Ultrason., Ferroelectr., Freq. Control*, vol. 63, no. 11, pp. 1922–1934, Nov. 2016.

[2] B. Denarie et al., "Coherent plane wave compounding for very high frame rate ultrasonography of rapidly moving targets," *IEEE Trans. Med. Imag.*, vol. 32, no. 7, pp. 1265–1276, Jul. 2013.

[3] G. Montaldo, M. Tanter, J. Bercoff, N. Benech, and M. Fink, "Coherent plane-wave compounding for very high frame rate ultrasonography and transient elastography," *IEEE Trans. Ultrason., Ferroelectr., Freq. Control*, vol. 56, no. 3, pp. 489–506, Mar. 2009.

[4] J. A. Jensen, S. I. Nikolov, K. L. Gammelmark, and M. H. Pedersen, "Synthetic aperture ultrasound imaging," *Ultrasonics*, vol. 44, Supplement, pp. e5–e15, Dec. 2006.

[5] M. Tanter and M. Fink, "Ultrafast imaging in biomedical ultrasound," *IEEE Trans. Ultrason., Ferroelectr., Freq. Control*, vol. 61, no. 1, pp. 102–119, Jan. 2014.

[6] V. Perrot, M. Polichetti, F. Varray, and D. Garcia, "So you think you can DAS? A viewpoint on delay-and-sum beamforming," *Ultrasonics*, vol. 111, Mar. 2021, Art. no. 106309.

[7] R. De Luca, L. Forzoni, F. Gelli, and J. Bamber, "An educational overview of ultrasound probe types and their fields of application," *Arch. Acoust.*, vol. 46, no. 1, pp. 3–15, Mar. 2021.

[8] T. L. Szabo and P. A. Lewin, "Ultrasound transducer selection in clinical imaging practice," *J. Ultrasound Med.*, vol. 32, no. 4, pp. 573–582, Apr. 2013.

[9] M. Couade, "The advent of ultrafast ultrasound in vascular imaging: A review," *J. Vasc. Diagn. Intervent.*, vol. 4, pp. 9–22, May 2016.

[10] M. S. Taljanovic et al., "Shear-wave elastography: Basic physics and musculoskeletal applications," *RadioGraphics*, vol. 37, no. 3, pp. 855–870, May 2017.
[11] L. Rocher et al., "Testicular ultrasensitive Doppler preliminary experience: A feasibility study," *Acta Radiologica*, vol. 59, no. 3, pp. 346–354, Mar. 2018.
[12] J. T. Yen, J. P. Steinberg, and S. W. Smith, "Sparse 2-D array design for real time rectilinear volumetric imaging," *IEEE Trans. Ultrason., Ferroelectr., Freq. Control*, vol. 47, no. 1, pp. 93–110, Jan. 2000.
[13] P. D. Wilcox and J. Zhang, "Quantification of the effect of array element pitch on imaging performance," *IEEE Trans. Ultrason., Ferroelectr., Freq. Control*, vol. 65, no. 4, pp. 600–616, Apr. 2018.
[14] R. S. C. Cobbold, *Foundations of Biomedical Ultrasound*. Oxford, U.K.: Oxford Univ. Press, Sep. 2006.
[15] O. T. von Ramm and S. W. Smith, "Beam steering with linear arrays," *IEEE Trans. Biomed. Eng.*, vol. BME-30, no. 8, pp. 438–452, Aug. 1983.
[16] A. Ponnle, H. Hasegawa, and H. Kanai, "Suppression of grating lobe artifacts in ultrasound images formed from diverging transmitting beams by modulation of receiving beams," *Ultrasound Med. Biol.*, vol. 39, no. 4, pp. 681–691, Apr. 2013.
[17] B. Delannoy, R. Torguet, C. Bruneel, E. Bridoux, J. M. Rouvaen, and H. Lasota, "Acoustical image reconstruction in parallel-processing analog electronic systems," *J. Appl. Phys.*, vol. 50, no. 5, pp. 3153–3159, May 1979.
[18] C. Bruneel, E. Bridoux, B. Delannoy, B. Nongaillard, J. M. Rouvaen, and R. Torguet, "Effect of spatial sampling on an acoustical image reconstruction," *J. Appl. Phys.*, vol. 49, no. 2, pp. 569–573, Feb. 1978.
[19] T. L. Szabo, *Diagnostic Ultrasound Imaging: Inside Out*, 2nd ed. Amsterdam, The Netherlands: Elsevier, Dec. 2013.
[20] J.-Y. Lu, H. Zou, and J. F. Greenleaf, "Biomedical ultrasound beam forming," *Ultrasound Med. Biol.*, vol. 20, no. 5, pp. 403–428, Jan. 1994.
[21] A. J. Devaney, *Mathematical Foundations of Imaging, Tomography and Wavefield Inversion*, 1st ed. Cambridge, U.K.: Cambridge Univ. Press, Jul. 2012.
[22] M. F. Schiffner and G. Schmitz, "Frequency-dependent F-number increases the contrast and the spatial resolution in fast pulse-echo ultrasound imaging," in *Proc. IEEE Int. Ultrason. Symp. (IUS)*, Sep. 2021, pp. 1–4.
[23] M. F. Schiffner and G. Schmitz, "A low-rate parallel Fourier domain beamforming method for ultrafast pulse-echo imaging," in *Proc. IEEE Int. Ultrason. Symp. (IUS)*, Sep. 2016, pp. 1–4.
[24] W. L. Briggs and V. E. Henson, *The DFT: An Owner's Manual for the Discrete Fourier Transform* (Other Titles in Applied Mathematics). Philadelphia, PA, USA: Society for Industrial and Applied Mathematics, 1995.
[25] S. Mallat, *A Wavelet Tour of Signal Processing: The Sparse Way*, 3rd ed. Cambridge, MA, USA: Academic Press, 2009.
[26] A. Rodriguez-Molares et al., "The ultrasound toolbox," in *Proc. IEEE Int. Ultrason. Symp. (IUS)*, Sep. 2017, pp. 1–4.
[27] J. Marini and J. Rivenez, "Acoustical fields from rectangular ultrasonic transducers for non-destructive testing and medical diagnosis," *Ultrasonics*, vol. 12, no. 6, pp. 251–256, Nov. 1974.
[28] I. Amidror, *The Theory of the Moiré Phenomenon* (Computational Imaging and Vision), 2nd ed. Berlin, Germany: Springer, Mar. 2009.
[29] J. Wojcik, M. Lewandowski, and N. Żołek, "Grating lobes suppression by adding virtual receiving subaperture in synthetic aperture imaging," *Ultrasonics*, vol. 76, pp. 125–135, Apr. 2017.
[30] A. Rodriguez-Molares et al., "The generalized contrast-to-noise ratio: A formal definition for lesion detectability," *IEEE Trans. Ultrason., Ferroelectr., Freq. Control*, vol. 67, no. 4, pp. 745–759, Apr. 2020.
[31] J. J. Stamnes, "Focusing of two-dimensional waves," *J. Opt. Soc. Amer.*, vol. 71, no. 1, pp. 15–31, Jan. 1981.
[32] I. K. Holfort, F. Gran, and J. A. Jensen, "Broadband minimum variance beamforming for ultrasound imaging," *IEEE Trans. Ultrason., Ferroelectr., Freq. Control*, vol. 56, no. 2, pp. 314–325, Feb. 2009.
[33] M. F. Schiffner. (2021). *Frequency-Dependent F-Number for Coherent Plane-Wave Compounding*. [Online]. Available: https://github.com/mschiffn/f_number
[34] S. Bae and T.-K. Song, "Methods for grating lobe suppression in ultrasound plane wave imaging," *Appl. Sci.*, vol. 8, no. 10, Oct. 2018, Art. no. 1881.
[35] M. Heller and G. Schmitz, "Reducing grating lobe artifacts by exploiting lateral transducer motion," in *Proc. IEEE Int. Ultrason. Symp. (IUS)*, Sep. 2020, pp. 1–4.
[36] Z. Kou, R. J. Miller, and M. L. Oelze, "Grating lobe reduction in plane-wave imaging with angular compounding using subtraction of coherent signals," *IEEE Trans. Ultrason., Ferroelectr., Freq. Control*, vol. 69, no. 12, pp. 3308–3316, Dec. 2022.
[37] L. W. Schmerr Jr., *Fundamentals of Ultrasonic Phased Arrays* (Solid Mechanics and Its Applications), vol. 215, 1st ed. Berlin, Germany: Springer, 2015.
[38] P. N. T. Wells, "Absorption and dispersion of ultrasound in biological tissue," *Ultrasound Med. Biol.*, vol. 1, no. 4, pp. 369–376, Mar. 1975.
[39] L. B. Felsen and N. Marcuvitz, *Radiation and Scattering of Waves* (Series on Electromagnetic Waves), 1st ed. Hoboken, NJ, USA: Wiley, Jan. 1994.
[40] F. W. J. Olver, D. W. Lozier, R. F. Boisvert, and C. W. Clark, *NIST Handbook of Mathematical Functions Hardback and CD-ROM*. Cambridge, U.K.: Cambridge Univ. Press, 2010.

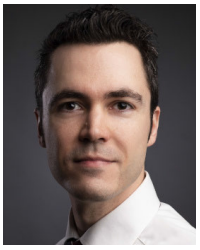

Martin F. Schiffner (Graduate Student Member, IEEE) received the Dipl.Ing. degree in electrical engineering and information technology from Ruhr University Bochum, Bochum, Germany, in 2008, where he is currently pursuing the Ph.D. degree with the Chair of Medical Engineering.

From 2006 to 2007, he was an ISAP Scholar at the Graduate School of Electrical and Computer Engineering, Purdue University, West Lafayette, IN, USA. He regularly publishes software on GitHub or tweets about his findings. His research focuses on computational ultrasound imaging (in particular the regularization of inverse scattering problems in fast ultrasound imaging), compressed sensing, diffraction tomography, beamforming, statistical signal processing, and wave propagation in heterogeneous media.

Mr. Schiffner is a member of the German Association of Electrical Engineers (VDE). He has served as a reviewer for multiple IEEE journals, including IEEE TRANSACTIONS ON ULTRASONICS, FERROELECTRICS, AND FREQUENCY CONTROL, IEEE TRANSACTIONS ON MEDICAL IMAGING, IEEE TRANSACTIONS ON IMAGE PROCESSING, and IEEE ACCESS. He was a finalist in the Student Paper Competition of the 2013 Joint IEEE International UFFC, EFTF, PFM Symposium, Prague, Czech Republic, where he won the IEEE Student Travel Support Award.

Georg Schmitz (Senior Member, IEEE) was born in Mülheim an der Ruhr, Germany, in 1965. He received the Dipl.Ing. and Dr.Ing. degrees in electrical engineering from Ruhr University Bochum, Bochum, Germany, in 1990 and 1995, respectively.

From 1995 to 2001, he was a Principal Scientist with the Philips Research Laboratories, Royal Philips Electronics, Hamburg and Aachen, Germany. From 2001 to 2004, he was a Professor of Medical Engineering with the University of Applied Science Koblenz, Koblenz, Germany. Since 2004, he has been a Professor of Electrical Engineering and the Chair of Medical Engineering with Ruhr University Bochum. His research interests are in the field of ultrasonic imaging and signal processing with current research projects on nonlinear image reconstruction, photoacoustic imaging, and super-resolution imaging using ultrasound localization microscopy.

Dr. Schmitz is a member of the Acoustical Society of America (ASA), the German Association of Electrical Engineers (VDE), and the World, European, and German Societies of Ultrasound in Medicine and Biology World Society of Ultrasound in Medicine and Biology (WFUMB), European Society of Ultrasound in Medicine and Biology (EFSUMB), and German Society of Ultrasound in Medicine and Biology (DEGUM). He is also a member of the Editorial Advisory Board of Ultrasound in Medicine and Biology. He served as an Associate Editor for the IEEE IEEE TRANSACTIONS ON ULTRASONICS, FERROELECTRICS, AND FREQUENCY CONTROL for 15 years.